Imperial College London

Appraisal of Pairwise Force Surface Tension Models for Smoothed Particle Hydrodynamics

Author:

Roger González

Supervisor:

Dr. Joaquim Peiró

A thesis submitted in fulfillment of the requirements for the degree of

MSc in Advanced Aeronautical Engineering

in the

Department of Aeronautics

June 5, 2018

Abstract

The main aim of this work is to identify a suitable surface tension model for a smoothed particle hydrodynamics code. The choices are reviewed according to accuracy, ability to capture variable wetting and suitability for large surface deformation. Akinci's comprehensive three part model is selected. To verify the model can replicate the characteristic behavior of surface tension three benchmark test cases are chosen, bubble formation, drop contact angle, and water crown formation. Issues highlighted with addition of the model are distorted pressure distribution, and boundary condition implementation. For the former, a solution in the form of a virial pressure is tested for hydrostatic conditions. The rigid boundary condition is corrected to eliminate the non-physical separation of the fluid from the wall. The cohesion of the fluid captures an overpressure inside a bubble true to the Laplace equation. Comparison of the evolution of the crown to a theoretically derived power law, found agreement to within 0.0008.

Acknowledgements

Contents

1. Introduction and Literature Review

The *aim* of this work is to appraise surface tension models for use in smooth particle hydrodynamics. Implementation of such a model is the logical next step in the development of a program to satisfy the current needs for modelling of fluid sloshing. The relevance of the problem discussed is outlined in this chapter, followed by a brief description of the underlying physics of surface tension. This builds the foundation on which the primary *objective* of this work can be fulfilled by selection, implementation and *verification* of a suitable model as presented in chapters 3 and 4.

1.1 Introduction

Surface tension is a force at the interface of different fluid phases and is a dominant feature in flows under compensated gravity. It can affect sloshing,the violent motion of a liquid in a partially filled container due to an external excitation. The fluid motion can quickly become highly non-linear and effect a large force on the container. The effect of surface tension on these flows is to change the local pressure near the surface and the distort of the macroscopic shape of the interface. The dynamics of sloshing are dependent on a wide range of variables including container geometry, excitation, liquid-fill depth and gravitational field. Hence the issue is relevant in engineering fields from the automobile industry and naval construction to aerospace [29]. The importance of this behavior is accentuated in transportation applications where the motion often interacts with the vehicles controls and structural dynamics. An outstanding example of these effects is that of the SpaceX Falcon 1 which tumbled out of control in March 2007. Flight telemetry reviews have confirmed that sloshing in the liquid oxygen tank caused the motion which the control system was unable to damp out. On earth, the gravitational field has stabilizing effect pulling the liquid volume to the bottom of the container [17]. This stability is characterized by higher than unity *Bond* and *Weber* number. Capillary effects are characterized by non-dimensional numbers, the *Bond* number and the *Weber* number. These can be derived by non-dimensionalising the Navier-Stokes equations with respect to the Laplace boundary condition [10]. The Bond number (Bo) describes the relative importance of surface tension and gravitational effects on the flow. The Weber (We) number is a measure of the relative dominance between inertial and surface tension forces.

$$Bo = \frac{\rho g L^2}{\sigma} \qquad (1.1) \qquad\qquad we = \frac{\rho v^2 L}{\sigma} \qquad (1.2)$$

where ρ is density, v the flow velocity, L is the characteristic length and σ is the surface tension.
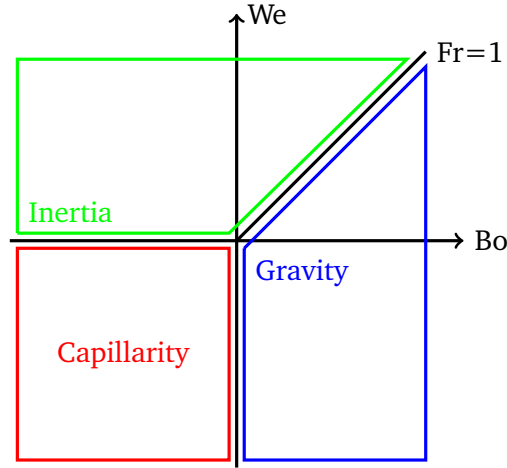
Figure 1.1: Hydrodynamic regimes origin=(1,1), $Fr = We/Bo$

For flows in varying gravitational fields the Bond number is most relevant. If $Bo \gg 1$, body forces dominate, for $Bo \ll 1$ the flow is capillary dominated, as is the case under compensated gravity. Regions in a Bond-Weber diagram are depicted in figure 1.1, where the origin of the graph represents the point where $Bo = We = 1$, as they cannot be negative. Under compensated gravity, body forces become almost negligible and capillary effects take over. These conditions cause behavior which is hard to replicate on earth. Liquids for example tend to adhere to the surfaces much more strongly. Studies of these dynamics have been outlined in a series of Technical Notes by NASA [7, 25, 26, 27, 28]. A review of these papers emphasizes the importance of capillarity in the design of storage tanks for space vehicles and some issues that may arise when the effects are not properly considered. For example, location of the liquid-vapour interface plays a key role in efficient and reliable pumping and venting of fluids in space. In propellant storage tanks, vapour pull-through could cause pump cavitation leading to catastrophic damage. Interface control also becomes important during reorientation maneuvers and docking, as violent sloshing can arise from relatively small excitations. Throughout these studies, it is hypothesized that proper employment of the surface tension properties of liquids could aid in control of the interface. This claim is supported in Dreyer's *Free surface Flows under compensated gravity conditions* where he states that:

Surface Tension forces can be used to transport and position liquids if the residual acceleration results in a hydrostatic pressure that is small compared to the capillary pressure.

Again pointing towards the effect of a drop in the Bond number of the flow. This statement serves as the cornerstone for the publication which outlines the advances in this field [10]. To facilitate future design of space-vehicles, free-fall experiments were designed which tested variables such as

container shape, filling percentage and contact angle. However, difficulties arose in the design of these experiments due to the free-fall conditions necessary which placed a tight constraint on the timescales and hence length scales. More recently an experiment carried out in the International Space Station called SPHERES-Slosh Experiment (SSE) studied these effects and gathered long term data of the fluid motion. The goal is to calibrate CFD programs with these data to accurately simulate coupled fluid-vehicle behavior in microgravity [20]. This will not only lead to reduced risk for space vehicles but can increase fuel efficiency here on earth. In simulating these phenomena issues emerge for established Computational Fluid Dynamics (CFD) methods due to the highly non-linear motion and multi-phase interactions at the free-surface. *Smoothed particle hydrodynamics* (SPH) is a fully Lagrangian method for solving the dynamical equations of fluids. SPH is a relatively young numerical method which shows promise for complex physics. Verifying the suitability of the method to accurately model the complex physics of surface tension pertinent to the sloshing problem is the primary goal of this work.

1.2 Surface Tension

Surface tension plays a significant role at the liquid-vapour inter-face in multi-phase systems. Surface tension or Capillary tension happens due to an imbalance in the molecular forces at the surface of a fluid. In the bulk of the fluid, each molecule is surrounded by similar molecules and the forces balance. The net force of a surface particle is the cohesion force and is in the direction of increasing density. The sum of the forces towards the bulk of the fluid create an over pressure in bubbles which can be described by the Laplace equation.

$$\Delta p = -\sigma \left(\frac{1}{R} + \frac{1}{R'} \right) \tag{1.3}$$

for an interface with radii of curvature R, R' and surface tension σ. The overpressure is responsible for properties of fluids such as the tendency of smaller bubbles to coalesce and capillary adhesion to solids.
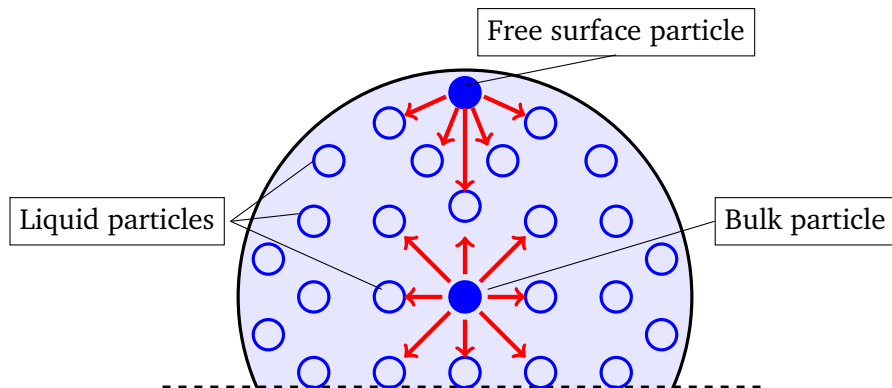
Considering a work balance on the surface of the liquid, at equilibrium, minimum surface areas satisfy Laplaces equation [9]. Note however, that surface area minimization is a result of surface tension forces and not its cause. A minimum surface area configuration would place the liquid surface in the lowest possible energy state for the given conditions. A similar force balance argument can be posed for solid-fluid interaction. At the triple point (solid-fluid-gas) this balance yields

$$\sigma \cos \theta = \sigma_{sg} - \sigma_{sl} \tag{1.4}$$

where σ_{sg} and σ_{sl} are the interacting forces between solid-gas and solid-liquid respectively. The wetting ability of the liquid can then be described by the contact angle θ which is conventionally measured through the liquid.

These forces are dominant at length scales smaller than the capillary length $k^{-1} = \sqrt{\sigma/\rho g}$ which, on earth, is in the order of millimeters for water. This relation arises by equating the Laplace pressure to the hydrostatic pressure in a liquid at a depth k^{-1}. Regarding k^{-1} as a screening length beyond which perturbations due to capillarity die down, the effect the gravity field has on these forces dominates. This can be visualized by comparing the meniscii of water in a glass container for different gravitational fields (Fig. 1.2) the profile of which is directly proportional to the capillary length as per

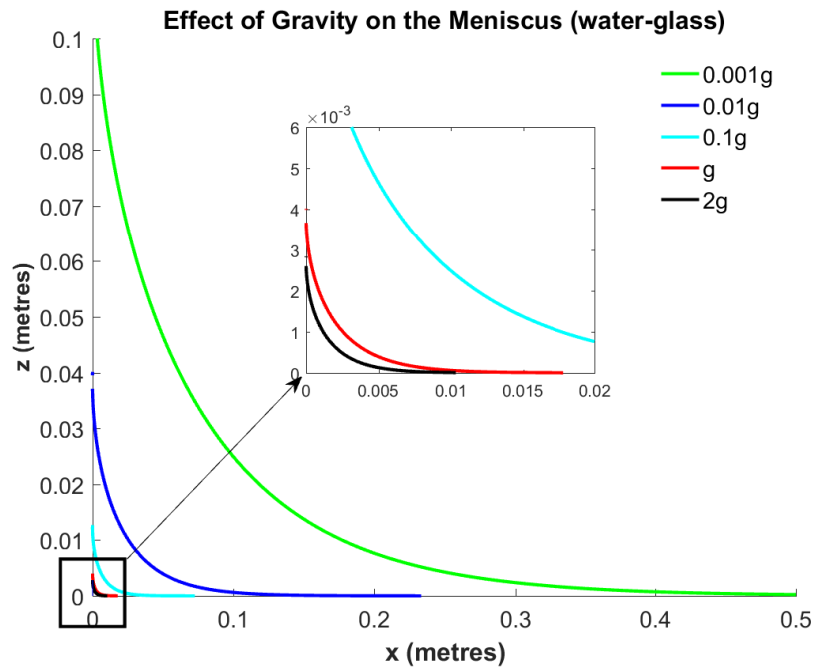$$x - x_0 = k^{-1} cosh^{-1}\left(\frac{2k^{-1}}{z}\right) - 2k^{-1}\left(1 - \frac{z^2}{4k^{-1}}\right)^{-1/2}$$

Figure 1.2: Profile of the meniscii formed at a water-glass interface in different gravitational fields.

A suitable model then would exhibit surface area minimization, adhesion of a liquid to a rigid surface as a function of the contact angle, and variation in strength of the capillary forces as a function of the capillary length, the Bond number and the Weber number. Note, the nature of the tension at the surface is wholly due to the cohesive forces inside the liquid. This is advantageous for numerical simulation as it suggests there is no need to model a second phase, which is computationally expensive.

1.3 Why SPH?

There are well established methods for computing the dynamical equations for fluids using meshed CFD. Namely, Finite difference (FDM), Finite Volume (FVM) and Finite element methods (FEM). However, for the case of fluid sloshing, complications arise. Violent motion at the free-surface makes surface tracking computationally expensive and mesh distortion and twisting may occur, affecting accuracy, [37]. The methods are categorised according to mesh type in table 1.1, the most significant distinction, [8].

For grid-based methods, attempts to simplify tracking of the interface include the level-set (LS) and volume of fluid (VoF) formulations. Introductions and reviews to different interface tracking approaches can be found in [31, 32]. Limitations arise with the proposed formulations for very small or very large surface tension which can result in conditions of significant density differences or under compensated gravity.

With respect to grid-based methods, Lagrangian deformable meshes offer implicit interface tracking. However the frequent re-meshing required adds significant computational overhead and complexity of implementation while at the same time decreasing accuracy, [31].

	Eulerian	Lagrangian
Grid-Based	Finite Difference Methods (LS,VoF,MAC,CIP)	Deformable Mesh
Meshless	FEM based on kernel approximations	Particle Methods

Table 1.1: Summary of the methods considered

Particle methods have the distinct advantage of ease in handling dynamically changing interfaces. They can be probabilistic such as Monte Carlo based molecular dynamics and the lattice Boltzman method, or determistic such as smoothed particle hydrodynamics (SPH) or the vortex method [21]. The lack of topologically stiff connections between nodes allows ease in local refinement, simple in-

terpolation and may provide more effective alternatives for paralellization. SPH is a fully Lagrangian particle method which offers distinct advantages for the simulation of free-surface flows and hence is the focus of this report.

In SPH the continuum is represented by a series of particles which offers the benefits of self-adaptability, ease in capturing the interface and natural concurrent computation[37]. Calculation of the fluid properties is carried out at each particle, thereby restricting the computational domain to the area of interest only, decreasing computational cost. In essence, the method is based on using a smoothing kernel to approximate the strong form of a partial differential equation (PDE) through a kernel based integral. SPH is particularly suited to free surface flows due to the fact that there is no need to impose a free-surface boundary condition if the weakly compressible formulation is applied.

In low-gravity applications, the inclusion of a second fluid phase may play a significant role [17]. Violent motion has been shown to overstep the assumptions necessary for the homogeneous model [13]. In these cases the relative velocity and hence forces occurring between fluid-phases play a significant role. Godderigge et al. show that with a finite volume formulation, the homogeneous model, which assumes relative motion between phases can be neglected, underestimates the experimental power spectrum by an order of magnitude [13]. Accuracy is also compromised for finite element formulations regardless of the liquid-gas density ratio [29]. In the inhomogeneous implementation, each fluid phase velocity field is resolved separately and matched at the interface using mass and momentum transfer [13]. Recently, SPH has proved to deal effectively with key features of multi-phase flows [37]. As oppose to the well established meshed methods, SPH lacks maturity and hence challenges remain in its implementation. Imposing a rigid boundary condition is often troublesome in particle based discretizations. Recent advances include the generalized wall boundary condition from Adami et al [2], and the γ-function boundary condition, a semi-analytical formulation recently improved by Ferrand et al [12]. A description of the boundary condition here implemented is given in section 2.3.

The last decade has brought many improvements to SPH. The method is characteristically suited for low Reynold's number flow involving complex geometries and multi-physics as any extra source term can be discretized separately and added to the momentum equation [33]. Finally, the explicit nature of the scheme makes it readily parallelizable. While it will not replace traditional meshed based CFD, the method in its current state-of-the-art is suitably positioned for the problem here discussed.

2. Smoothed Particle Hydrodynamics

The following is a brief outline of the formulation used in this study as derived by Violeau in [36] and implemented by Eichstadt [11].

2.1 SPH operators and Kernel interpolation

To accurately model the governing equations computationally requires an approximation of spatial derivatives from a finite number of points. The SPH method makes use of an integral interpolant of the form 2.1 to approach a quantity f at position $\mathbf{x}$. The interpolant reproduces f exactly if the kernel W is a Dirac-delta function. For practical reasons, the Dirac distribution is instead approached through a regular function, here-on referred to as a kernel, with non-zero values within a compact support and zero everywhere else, confining the integration over a finite domain Ω. The interpolant, its gradient and a divergence operator can be approximated as Riemann sums over a finite domain N. This reveals one of the advantages of SPH where the derivative of a function can be approximated using only the derivative of the kernel $\nabla_a W_{ab}$. It is within this framework that the governing equations of fluids are discretized.

<div align="center">Interpolation integral</div>

$$f(\mathbf{x}) \approx \int_\Omega f(\mathbf{y}) W(\mathbf{x} - \mathbf{y}, h) d\mathbf{y} \qquad (2.1) \qquad\qquad \langle f(\mathbf{x}_a) \rangle = \sum_b^N V_b f(x_b) W_{ab} \qquad (2.2)$$

<div align="center">Gradient Operator</div>

$$\nabla_x f(\mathbf{x}) \approx \int_\Omega f(\mathbf{y}) \nabla_x W(\mathbf{x} - \mathbf{y}, h) d\mathbf{y} \qquad (2.3) \qquad\qquad \langle \nabla f(\mathbf{x}_a) \rangle = \sum_b^N V_b f(x_b) \nabla_a W_{ab} \qquad (2.4)$$

<div align="center">Divergence Operator</div>

$$\nabla_x \cdot f(\mathbf{x}) \approx \int_\Omega f(\mathbf{y}) \nabla_x \cdot W(\mathbf{x} - \mathbf{y}, h) d\mathbf{y} \qquad (2.5) \qquad\qquad \langle \nabla \cdot f(\mathbf{x}_a) \rangle = \sum_b^N V_b f(x_b) \cdot \nabla_a W_{ab} \qquad (2.6)$$

where a is the particle in question and b is a neighboring particle. The current discrete formulations for the operators are not symmetric or anti-symmetric, required features for the conservation equations. Considering the weakly compressible formulation desired, and conservation of momentum, Eichstadt limits the choice of operators to symmetric divergence operators (2.8) and anti-symmetric gradient operators (2.7) [11].

$$\nabla f(x_a) = \sum_b V_b \frac{\rho_b^{2k} f(x_a) + \rho_b^{2k} f(x_b)}{(\rho_a \rho_b)^k} W_{ab}' e_{ab} \qquad (2.7)$$

$$\nabla \cdot f(x_a) = -\frac{1}{\rho_a^{2k}} \sum_b V_b (\rho_a \rho_b)^k (f(x_b) - f(x_a)) \cdot W'_{ab} e_{ab} \tag{2.8}$$

where $W'_{ab} e_{ab} = \nabla_a W(x_a - x_b, h)$ and is the gradient of the kernel. The choice of kernel is dependent on satisfying the certain conditions. The need for symmetric operators with anti-symmetric gradients imposes the same constraint on the kernel. There is a variety of smoothing kernels to choose from, which yield different accuracy and computational efficiency. Wan et al. list the full requirements for the kernel function and suggests various versions [37]. In general, kernel functions are defined as

$$W(x - y, h) = \frac{\alpha_d}{h^d} f(r) \tag{2.9}$$

Where $r = \frac{|x-y|}{h}$ is a dimensionless function of the spatial distance between two points, α_d is a scaling factor, d is the spatial dimension, and h is the initial inter particle distance. The quintic B-spline (2.10) is chosen for this work. The relatively large support domain ($3h$) of this function improves interpolation accuracy and stability. While this same feature increases computational cost, prioritizing accuracy is deemed imperative for the boundary conditions implemented.

$$f(r) = \begin{cases} (3-r)^5 - 6(2-r)^5 + 15(1-r)^5 & 0 \leq r \leq 1 \\ (3-r)^5 - 6(2-r)^5 & 1 < r \leq 2 \\ (3-r)^5 & 2 < r \leq 3 \\ 0 & 3 < r \end{cases} \tag{2.10}$$

2.2 Discretization of the governing equations

The governing equations of fluid dynamics are the Navier-Stokes, which under the assumption that $\nabla \cdot u = 0$ and in Lagrangian form are:

$$\frac{D\rho}{Dt} = -\rho \nabla \cdot \mathbf{u} \tag{2.11}$$

$$\frac{D\mathbf{u}}{Dt} = -\frac{1}{\rho} \nabla p + \nu \nabla^2 \mathbf{u} + \mathbf{f}_{ext} \tag{2.12}$$

where $\frac{D}{Dt}$ is the material derivative, $\mathbf{u}$ is the velocity vector, ρ is the density, p is the pressure, ν is the kinematic viscosity and $\mathbf{f}_{ext}$ is an external force. In this model, a weakly compressible flow is considered and thermal effects are excluded, hence the viscosity stays constant and may also be neglected. The inviscid momentum equation is the Euler equation

$$\frac{D\mathbf{u}}{Dt} = -\frac{1}{\rho} \nabla p + \mathbf{f}_{ext} \tag{2.13}$$

Eichstadt argues that for the case of multi-phase flows with steep density gradients, an adaptation to the general SPH operators is best suited and opts for the formulation (2.14), (2.15) for the continuity and momentum equations respectively. The derivations for which can be found in [15].

$$\frac{D\rho_{\mathbf{a}}}{Dt} = \rho_a \sum_b V_b(\mathbf{u}_a - \mathbf{u}_b)\tilde{p}_{ab} W'_{ab} \mathbf{e}_{ab} \tag{2.14}$$

$$\frac{D\mathbf{u}_{\mathbf{a}}}{Dt} = -\frac{1}{m_a} \sum_b (V_a^2 + V_b^2)\tilde{p}_{ab} W'_{ab} \mathbf{e}_{ab} + \mathbf{f}_{ext} \tag{2.15}$$

where

$$\tilde{p}_{ab} = \frac{\rho_b p_a + \rho_a p_b}{\rho_a + \rho_b}$$

The SPH equations are closed with the constitutive relation for weakly compressible fluids

$$p = \frac{\rho_0 c_0^2}{\Gamma}\left[\left(\frac{\rho}{\rho_0}\right)^{\Gamma} - 1\right] \tag{2.16}$$

where ρ_0 and c_0 are reference density and pressure respectively. $\Gamma = 7$ for water and is a parameter that must be calibrated for each fluid.

2.3 Boundary Conditions

Boundary condition implementation is an ongoing battle in SPH. The SPHERIC community, which spearheads SPH development, considers it one of the grand challenges for improving the method. In this work a weakly-compressible SPH scheme was selected which removes the need to impose a free-surface boundary condition. Solid boundaries present an ongoing challenge with four main methods offering current state of the art solutions; boundary particle force model, image particle model, dynamic particle model and semi-analytical model for which there is extensive literature [11, 36, 37]. A dummy particle method is selected for this work due to its ease of implementation, accuracy in capturing the pressure field near the wall and low computational cost. The method is based on a force balance at the wall from which a pressure force is calculated in order to maintain the impermeability condition of rigid walls. For a wall particle p_w under the influence of multiple fluid particles p_f the pressure force is

$$p_w = \frac{\sum_f p_f W_{wf} + \sum_f \rho_f \mathbf{g} \cdot (\mathbf{x_w} - \mathbf{x_f}) W_{wf}}{\sum_f W_{wf}} \tag{2.17}$$

The method has been validated for Poiseuille and Couette flows and under free-fall conditions instilling confidence in its efficiency and applicability for micro-gravity conditions [2].

2.4 Time Integration

A symplectic time integration algorithm as discussed by Violeau is implemented [36]. This category of time integration is particularly suited for SPH applications as it is energy conserving while being relatively simple to implement.

$$\mathbf{u}_a^{n+1/2} = \mathbf{u}_a^n + \frac{\Delta t}{2}\left(\frac{D\mathbf{u}_a}{Dt}\right)^n \tag{2.18}$$

$$\mathbf{x}_a^{n+1/2} = \mathbf{x}_a^n + \frac{\Delta t}{2}\mathbf{u}_a^{n+1/2} \tag{2.19}$$

$$\rho_a^{n+1} = \rho_a^n + \Delta t\left(\frac{D\rho_a}{Dt}\right)^{n+1/2} \tag{2.20}$$

$$\mathbf{x}_a^{n+1} = \mathbf{x}_a^{n+1/2} + \frac{\Delta t}{2}\mathbf{u}_a^{n+1/2} \tag{2.21}$$

$$\mathbf{u}_a^{n+1} = \mathbf{u}_a^{n+1/2} + \frac{\Delta t}{2}\left(\frac{D\mathbf{u}_a}{Dt}(\rho_a^{n+1})\right)^{n+1} \tag{2.22}$$

The time step, Δt is evaluated at each iteration according to three conditions; a CFL-condition, a field-force condition and a viscous condition. The choice of surface tension model can affect this condition. It is noticed that Akinci's model produces relatively large forces and hence velocities. While this means the flow exhibits more realistic behavior, the time step is constraint by a larger maximum velocity according to the CFL-condition.

$$\Delta t \le 0.25\frac{h}{c_0 + \|u_{max}\|} \tag{2.23}$$

$$\Delta t \le 0.25\left(\frac{h}{\|g\|}\right)^{1/2} \tag{2.24}$$

$$\Delta t \le 0.125\frac{h^2}{\nu} \tag{2.25}$$

2.5 Viscocity

Although not strictly necessary for the test cases here shown, a viscosity term is added to to SPH formulation for numerical stability. This is because the inviscid momentum equation has been found to be unstable. The viscocity term $\mathbf{F}^\nu$ is added to the right hand side of the momentum equation.

$$\mathbf{F}^\nu = -\sum_b \alpha hc\frac{m_b}{\rho_{ab}}\frac{(\mathbf{v}_a - \mathbf{v}_b)\cdot(\mathbf{x}_a - \mathbf{x}_b)}{(\mathbf{x}_a - \mathbf{x}_b)^2 + \epsilon h^2}W'_{ab}\mathbf{e}_{ab} \tag{2.26}$$

where α is the artificial viscosity parameter, $\rho_{ab} = (\rho_a + \rho_b)/2$ is the density average of the two particles and parameter $\epsilon = 0.01$ is included to avoid division by zero. The force is only applied for particle pairs which are moving towards each other.

3. Numerical Models for Surface tension

The *objective* of this chapter is to identify a suitable surface tension model for SPH. The following outlines an assesment of the common choices. Aiming to accurately simulate liquid behavior across different scales and conditions, the ability of a model to maintain accuracy for particles with incomplete neighborhoods is prioritized.

3.1 Surface Tension Models for SPH

There exists three families of models for surface tension in SPH applications. Namely, the cohesive pressure (CP), the pairwise force (PF), and the continuum surface force (CSF) models [37].

In general, the family of CP and PF models deal with the interacting forces between particles. These models assume that the interfacial tension can be described by the interaction of molecular particles alone.

In CSF, the force per unit surface area (f_s) is found through application of the Young-Laplace boundary condition then treated as a body force in the momentum and continuity equations [37].

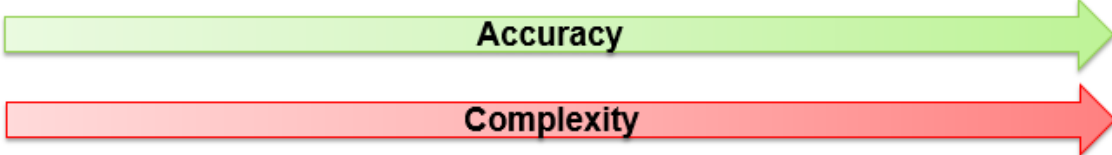$$f_s = \sigma k \boldsymbol{n} + \nabla_s \sigma \tag{3.1}$$

In this respect it deals with macroscopic parameters; the surface tension σ and curvature k of the surface. The second term is the gradient of the surface tension at the surface which is analogous to the tangential pressure in the macroscopic analytical derivation for surface tension. Although in general they are more accurate, the CSF models are computationally expensive requiring the calculation of the interface or free surface curvature. This method has previously been implemented using surface reconstruction to compute the curvature [1]. The nature of this calculation means the CSF model cannot adequately handle large curvature, which is expected in violent sloshing motions, due to the sensitivity of the calculation to particle distribution. Another method of calculating the gradient is the use of a color function. In essence the color function is an indexing method where each fluid phase is characterized by an integer assigned to each particle of that fluid. The gradient of the color function of a particle then is calculated by a weighted average of the color of its neighborhood. However, this method is affected by small particle populations which are expected at the surface.

CP models are based on using the Van-der-Waals equation of state relating pressure to density

$$p = \frac{\rho k_B T}{1 - \rho b} - a \rho^2 \tag{3.2}$$

where k_B is the Boltzmann constant, b is a constant per unit mass due to the finite volume of particles, and a is the strength of the cohesive forces per unit mass between molecules. The second term in equation 3.2 represents the cohesive force between neighboring particles. This pressure force is balanced and hence eliminated in the bulk of the fluid, taking effect only near the surface. The Laplace relation (1.3) is then used to calculate the surface tension. The simplicity of this model leads to numerical instabilities if the range of the interaction is not significantly increased, increasing computational cost [24].

	Cohesive Pressure	Pairwise Force	Continuous Surface Force
Scale	Microscopic	Microscopic	Macroscopic
Principle	Van der Waals forces	Inter-molecular forces	Proportional to curvature
Features	• Large smoothing length • Calibration • Don't guarantee surface area minimization • Pressure distortion	• Calibration • Don't guarantee surface area minimization • Can avoid particle clustering • Variable wettability	• Complex surface tracking • Not accurate for large deformation • No calibration • Guarantees surface area minimization

Accuracy →

Complexity →

Figure 3.1: Summary of the three most pupolar types of surface tension models for Smoothed Particle Hydrodynamics.

Given the superior quality and versatility with respect to the CP model, and simplicity relative to the CSF, the pairwise-force model is selected for further study. It has the key advantage of being easily generalized to fluid-structure interaction, a key feature for the simulation of fluid sloshing in a vessel. Difficulties arise concerning the accuracy because certain parameters for these models needs to be calibrated through numerical experiment. However, recent work have arrived at analytically derived relations between the values of pairwise-forces and macroscopic values for surface tension and contact angle [35, 23]. While there is no established model for PF, the following summarizes some popular choices, and builds on the critique offered by Wang et al. [37].

3.2   SPH and Molecular Dynamics

It is worth noting that in real multi-phase flows, the forces which cause surface tension act between molecules and hence are molecular in scale. SPH however, assumes that the behavior can be mimicked in a macroscopic scale [6]. This is in keeping with W.G Hoover's claim that SPH is *isomorphic* with molecular dynamics [38]. That is, the macroscopic dynamics of smoothed particles for many particle interactions is exactly identical to the molecular dynamics of a dense fluid under a pair potential force. This statement holds for certain formulations where the combination of the equation of state and the discretized form of the pressure gradient result in the governing of the evolution of the particle by the kernel function alone. For example, taking equation 2.7 for $f(x) = p$ and letting $k = 1$ yields

$$\frac{D\mathbf{u}_a}{Dt} = -\sum_b m_d\left(\frac{p_a}{\rho_a^2} + \frac{p_b}{\rho_b^2}\right)W'_{ab}\mathbf{e}_{ab} + \mathbf{f}_{ext} \tag{3.3}$$

Then if the pressure is proportional to the density squared $p \propto \rho^2$, the momentum equation is a function of the gradient of the kernel function alone. Which is exactly the same form of the governing equation of motion for molecular dynamics[38]. For other equations of state, the relation is not exact. On the other hand, Hoover and Hess argue that whenever the pressure and density are approximately constant, the continuum as represented by smooth particles, obeys the motion equations of conventional molecular dynamics [14]. In this respect, the treatment of the macroscopic dynamics of smoothed particles is consistent with that of particles in molecular dynamics and can be modelled as pair potentials.

3.3   Pairwise Force Models

PF-SPH models approximate the inter-molecular forces between liquid particles. In general they are of the form:

$$F_a = \sum_b^N F_{ab}(\mathbf{r}_{ab}) \tag{3.4}$$

where a is the particle in question, b is a particle inside its support, F_{ab} is the interaction force and r_{ab} is the distance between the particles. F_a is added to the right hand side of the momentum equation. While the shape of the pairwise interaction force F_{ab} varies, it should exhibit similar dynamics to the molecular interaction, that is short-range repulsive and long range attractive. Further, in order to conserve momentum the force should be anti-symmetric. The form of the pairwise force affects the distribution of the particles, which affects the accuracy for all SPH parameters. For the sake of

computational efficiency the force should be zero for a distance between particles a and b greater than the kernel support [19].

The Lennard-Jones potential is a commonly used function describing the interaction between molecules. This model has been extensively investigated and has the added benefit of being simple to implement in an SPH context. This formulation however is not anti-symmetric which implies conservation of momentum is not obeyed. Further it is a stiff force and will constrain the time step [37].

Tartakovsky and Meakin propose a cosine formulation for the pairwise-force [34], upon which Tartakovsky and Pachenko later build on presenting four different descriptions of the force F_{ab} ,[35]. Further, the need for numerical calibration of the constant $s_{\alpha\beta}$, which determines the magnitude of the tensile interaction between phases α and β, can negatively affect the accuracy of the SPH implementation. Two new models are suggested which decrease the clustering exhibited by the cosine force [35]. Their formulation is based on the superposition of two gaussian functions which makes implementation simple while keeping computational cost low. These models require the modelling of a second phase.

Kordilla et al. suggest a function consisting of two superposed kernels which result in properties suitable for this application [19]. This model has increased computational cost and maintains the need to be calibrated.

Akinci et al. [3] derive separate functions for liquid cohesion, surface area minimization and fluid-solid interaction. This allows the use of both pairwise-forces and continuum surface forces the combination of which leverages the strengths of both these methods. The surface tension force is repulsive at close range, decreasing particle clustering [3]. Based on a spline function, this force closely mimics the molecular potential, and is fully anti-symmetric:

$$F_{ab}^{cohesion} = -\gamma m_a m_b C(r_{ab}) \frac{\mathbf{r}_{ab}}{r_{ab}} \quad , \quad C(r) = \frac{32}{\pi(kh)^9} \begin{cases} (kh-r)^3 r^3 & 0.5kh \le r \le kh \\ 2(kh-r)^3 r^3 - \frac{(kh)^6}{64} & 0 \le r < 0.5kh \\ 0 & otherwise \end{cases} \quad (3.5)$$

where γ is the cohesion coefficient, m_a and m_b are particle masses, h is the smoothing length and kh is the kernel support. PF models alone do not guarantee surface area minimization as the forces may balance in other configurations [37]. An extra surface area minimization term, the *curvature* term, is added which avoids calculation of the surface curvature explicitly which, as discussed, is both computationally expensive and inaccurate for violent motion in SPH. It is based on the gradient of a color function, n_a, which is null in the bulk of the fluid and is proportional to the curvature, hence

maximum at the surface.

$$F_{ab}^{curvature} = -\gamma m_a(\mathbf{n}_a - \mathbf{n}_b) \quad , \quad \mathbf{n}_a = kh\sum_b \frac{m_b}{\rho_b}\nabla_a W_{ab} \tag{3.6}$$

Fluid-Solid interactions are described by a steep parabolic function in a third force, the *adhesion* force.

$$F_{ab}^{adhesion} = -\beta m_a \Psi_{b_k} A(r_{ab})\frac{\mathbf{r_{ab}}}{r_{ab}} \quad , \quad A(r) = \frac{0.007}{kh^{3.25}}\begin{cases} \sqrt[4]{-\frac{4r^2}{kh} + 6r - 2kh} & 0.5kh \leq r \leq kh \\ 0 & otherwise \end{cases} \tag{3.7}$$

where Ψ_{b_k} is the volume of a boundary particle based on its sampling density, which adheres to the concept in SPH of field variable proportionality to particle volume [4].

$$\Psi_{b_k}(\rho_0) = \frac{\rho_0}{\sum_k W_{bk}} \tag{3.8}$$

where ρ_0 is the static fluid density, b is a boundary particle, and k is a nieghbouring boundary particle. This formulation achieves versatility in modeling different wetting conditions while avoiding clustering and unphysical separation near the boundary when coupled with the rigid-fluid boundary condition suggested [3, 4]. The complete set of forces then comprehensively model the physics. While computationally more expensive than the pairwise force alone, Akinci et al. achieve remarkable results commending serious consideration for implementation in this work.

Issues arise in SPH for particles at the free surface for particles whose kernel domain may not be fully populated. To solve this issue, a correction factor K_{ab} is suggested which amplifies the surface tension forces for a particle with neighborhood deficiency [3].

$$K_{ab} = \frac{2\rho_0}{\rho_a + \rho_b} \tag{3.9}$$

where ρ_0 is the reference fluid density, and ρ_a, ρ_b are the densities of the particle in question and a neighboring particle respectively. The full surface tension force is then

$$F_{ab} = K_{ab}(F_{ab}^{cohesion} + F_{ab}^{curvature}) + F_{ab}^{adhesion} \tag{3.10}$$

3.3.1 Discussion

Figure 3.2 presents the shape of the discussed pairwise forces in a unit domain. All forces shown exhibit behavior reminiscent of the underlying molecular force, that is, long-range attractive and short-range repulsive. Huber et al. carry out an evaluation of the cohesion effects of these models in an attempt to establish benchmark tests for surface tension in SPH [16]. In order to maximize accuracy under large deformation and achieve variable wetting behavior, Akinci's three-part model is

chosen. The model is included in Huber's evaluation in which it is regarded as the most physically representative [16]. Adhesion effects in rigid-fluid interactions have not been widely studied for SPH. This is due to the difficulties which arise in treatment of the boundary condition. These effects become increasingly important under compensated gravity as liquids adhere more strongly to the surfaces. Therefore, the ability to simulate a variety of wetting conditions is important to this work, and Akinci's model has been shown to do this effectively. All the forces involved in this model are fully anti-symmetric thereby momentum conserving, a key aspect in keeping with the assumption in the derivation of the SPH formulation. Violent motion of the free-surface is expected in sloshing. As discussed, CSF models alone are inaccurate in these conditions. The superposition of the cohesion and curvature terms in this model alleviates this loss in accuracy. Further, it allows modelling of the effects of surface tension without the need for a seconds phase, minimizing computational cost. The physical cause of surface tension is the cohesion forces inside the fluid and hence the fluid should exhibit tensile behavior at the surface even when no second phase is explicitly simulated [3]. Akinci's model seems to overcome many of the constraints of the CSF and PF models alone.
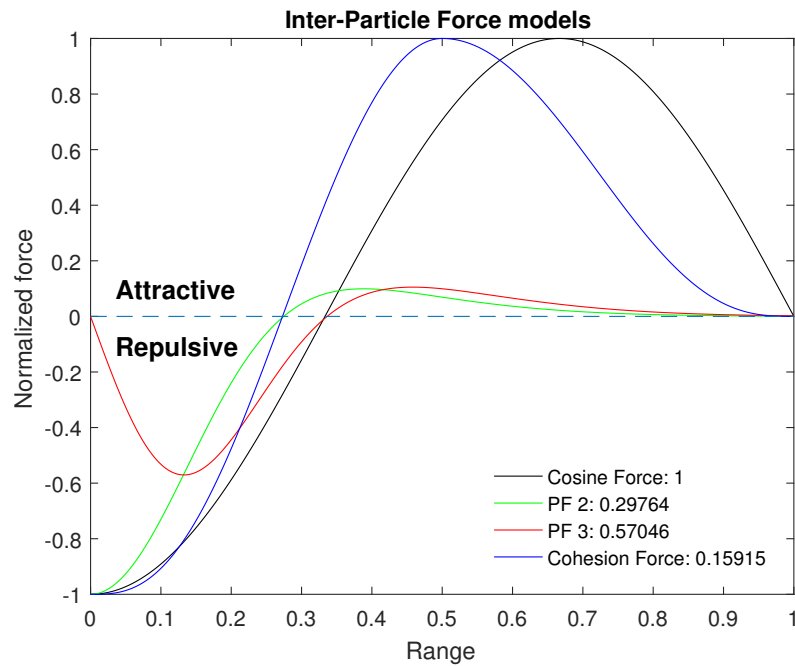
Figure 3.2: Shape of the normalized pairwise forces with non-normalized magnitude in legend. Cosine force [34], PF 2 and PF 3 refer to the gaussian function forces [35], cohesion force is part of the implemented model [3]. The range represents the inter-particle distance

4. Simulation Results and Discussion

This chapter outlines the *verification* of the chosen model. Benchmark test cases are simulated to this aim which showcase the surface tension effects implemented in this work. Liquid cohesion and surface area minimization are tested in a bubble formation simulation. Variable liquid to solid adhesion is calibrated and tested by a droplet contact angle measurement. The effect of the addition of this model to the existing SPH implementation is quantified by comparing the hydrostatic pressure distribution with the added surface tension. Issues arise when the surface tension term interacts with a solid boundary. A solution is described for the case of drops on a flat surface. The model can finally be *validated* against theoretically derived relations using a crown evolution test case.

4.1 Time step considerations due to Pairwise forces

The addition of extra force terms to the SPH formulation can cause stability issues. Already SPH is unstable and with Akinci's model the forces involved become larger. Stability issues arose for simulations which involved very high particle resolution at high densities. For the bubble formation test case for example, particles would be launched out in the initial stages as the accelerations would be extremely large. A solution to this is to employ a type of *Courant-Friedrichs-Lewy* (CFL) condition for the forces involved as recommended by Ihmsen et al. [18]. In SPH the CFL condition constrains the time step so that a particle is not displaced more than its smoothing length in a single time step. The additional forces in the form of the pairwise forces will create higher acceleration and the authors suggest creating a new time step constrain with respect to this condition.

$$\Delta t \leq \lambda_f \left(\sqrt{\frac{h}{F_{max}}} \right) \tag{4.1}$$

where λ_f is a coefficient suggested to be 0.25 by Monaghan [22], h is the smoothing length, and F_{max} is the maximum force experienced by a particle in a given a time step. Bubble simulation tests for this condition yields a neglegible change in the minimum time step for a $\gamma = 1$ and $\Delta x = 0.01$. The conditions in place are sufficient to maintain stability. This is in keeping with the *soft*, i.e. finite magnitude for an inter particle distance of zero, nature of pairwise forces [35].

4.2 Bubble formation

One of the key phenomena attributed to surface tension is the tendency of liquids to minimize their surface area. This feature is tested by allowing a bubble to form under zero gravity conditions from

an initially square domain. The simulation is allowed to reach a state where the macroscopic shape of the fluid does not change. However, a full steady state is not expected as that would imply zero energy for an SPH formulation. The pressure field is quantified with respect to a reference pressure $p_{ref} = \rho_0 \|g_y\| H$. For bubbles in "zero" gravity, a value of $g_y = -1.0$ is used while the actual gravitational force is omitted from the momentum equation. This values is necessary for the determination of the artificial speed of sound defined as $c = 10 v_{ref}$ where $v_{ref} = \sqrt{|g| H}$. H in this case is the height of the initial square domain. The artificial viscosity coefficient $\alpha = 0.24$. The maximum velocity is found by calculating the absolute velocity $v = \sqrt{v_x^2 + v_y^2}$ of each particle at each time step saved, and finding the maximum. For all the simulations which follow, the volume of a particle is $V = \Delta x^2$ and the reference density is $\rho_0 = 1000$ unless explicitly stated otherwise.
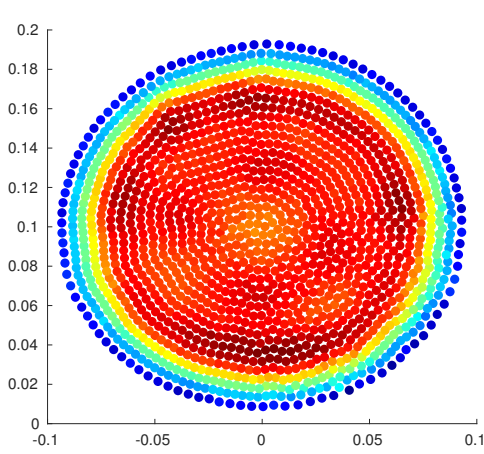
Figure 4.1: Final Bubble equilibrium with pressure distribution (pairwise force only)
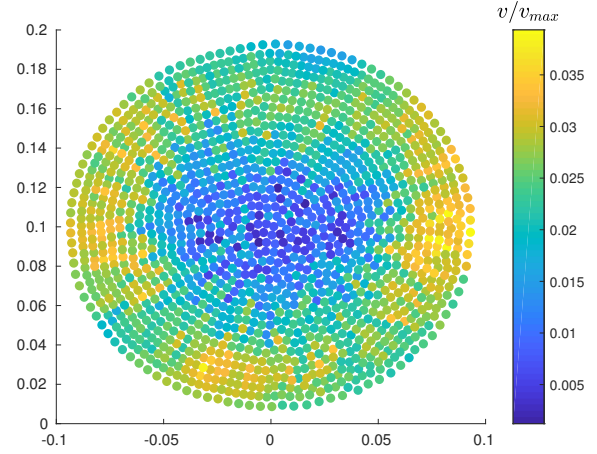
Figure 4.2: Final Bubble equilibrium with residual velocity distribution (pairwise force only)
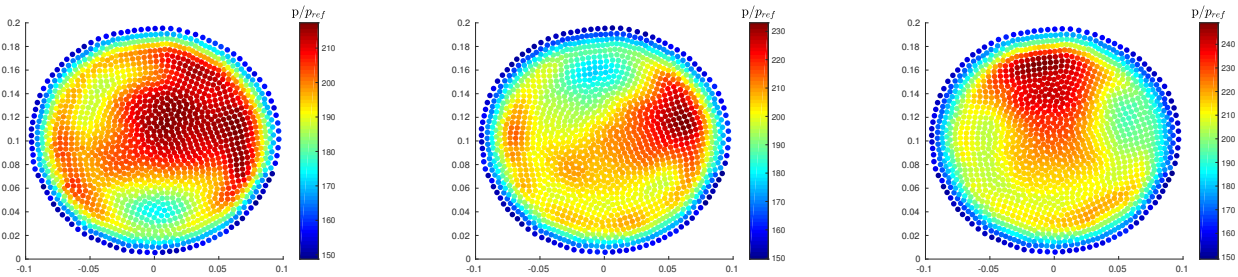
Figure 4.3: Oscillating pressure distribution in final time steps for fully integrated pairwise force with CSF

This model is a mixture of the pairwise and continuous surface forces. To test the effect of each force, simulations are carried at with only the Pairwise force term, and then both terms together. The CSF

alone is found to be too small to properly model the physics. The large forces characteristic of this model deform the fluid very quickly. This can be more clearly illustrated in a video which can be found here. This causes large pressure and velocity values throughout the initial stages of the simulation, which constrain the time step. In the last fifty time steps, the particles oscillate around their position, but the overall shape of the bubble does not change. Figure 4.1 shows the pressure distribution of a free bubble with the pairwise force contribution only. Evidently, the model has captured the overpressure exhibited by bubbles according to Laplace's equation 1.3. Without inclusion of the CSF, it has minimized the area effectively (Fig.4.4). The minimization of the area is measured by the circularity of the final bubble. For a perfect circle, the radius in every direction would be the same. In this case the outermost particles are taken and their distance from the center of the bubble as a function of the angle is calculated. The standard deviation represents the average distance away from the mean. In this case, how close the bubble is to a perfect circle. Figure 4.3 depicts the pressure distribution in a bubble, under both the pairwise and CSF forces, as it approaches equilibrium. The overpressure towards the center is captured. However, the larger forces due to the inclusion of both terms cause the pressure distribution to oscillate rapidly. With respect to the pairwise forces alone, the combination of CSF and PF has been less effective in minimizing the surface area (Fig.4.5).
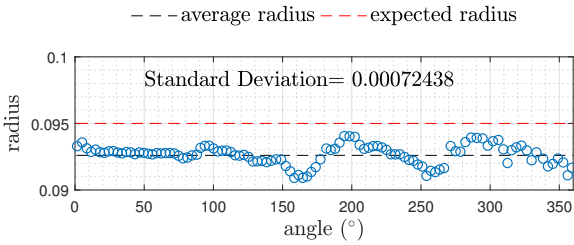

Figure 4.4: distribution of the radius around the bubble with pairwise forces alone
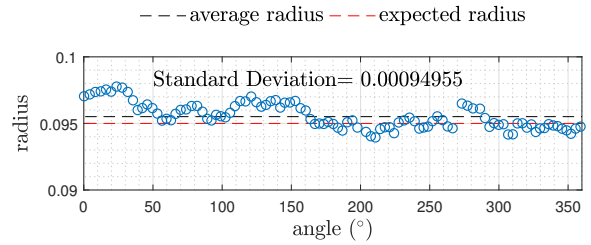

Figure 4.5: distribution of the radius around the bubble with pairwise forces and CSF

In this work the Laplace equation is used to measure the surface tension σ. This particular model does not require a second phase to be simulated in order to achieve surface tension keeping computational cost low. This is in keeping with the nature of surface tension which, as explained, is due to the cohesive forces within the liquid. Bubbles of different radii are initialized in a Cartesian grid and allowed to evolve to an equilibrium position. The internal pressure of the bubble is measured from a SPH average of the particles within a kernel support distance of the centre of the bubble. The equilibrium radius is calculated as the average of the radius in the x and y direction. Fig.(4.6) finds the surface tension from a regression of simulations of bubbles of different radii. An approximation

of the simulated surface tension is given by the slope of the regression line according to Laplace's equation $P = \frac{\sigma}{R}$. For $\gamma = 1$, and radii $0.05 < r < 0.2$ a value for the surface tension $\sigma = 0.019064$ is calculated.
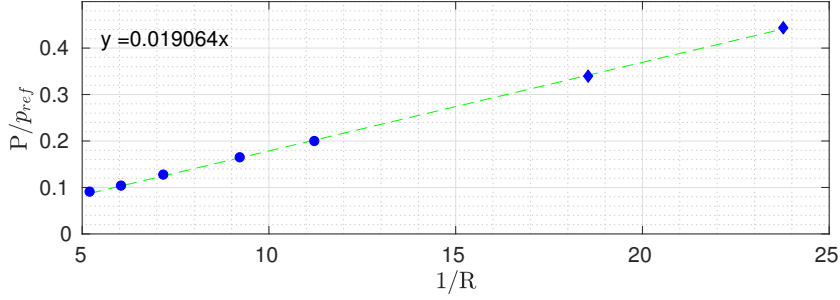

Figure 4.6: Observed change in non dimensional pressure for bubbles of different radii $\gamma = 1$, (circle=$\Delta x = 0.01$),(diamond=$\Delta x = 0.005$)

4.2.1 Dynamic bubble

To study the dynamic behavior of the surface tension for bubbles under zero gravity, an oscillating bubble is simulated. The domain is initialized in square Cartesian grid of size 0.2 with $\Delta x = 0.01$ yielding 400 particles. The fluid, with prescribed density $\rho_0 = 1000$, is allowed to reach circular equilibrium and is then deformed into an ellipse with eccentricity $e = 0.7$ using an area preserving particle coordinate transformation, thereby conserving density and mass [24].

$$\begin{pmatrix} x' \\ y' \end{pmatrix} = \sqrt{\frac{2}{\sin\phi}} \mathbf{r} \begin{pmatrix} \sin(\frac{\phi}{2})\sin u \\ \cos(\frac{\phi}{2})\cos u \end{pmatrix} \tag{4.2}$$

where $\mathbf{r} = \sqrt{x^2 + y^2}$, $u = \arctan(x/y)$ and $\phi = e\pi$. The simulation is then evolved and, as the bubble oscillates, the evolution of the radii in the x and y direction are tracked (Fig.4.7). For oscillation of small amplitude the surface tension σ can be calculated from the period of oscillation τ by

$$\tau = 2\pi\sqrt{\frac{R^3\rho}{6\sigma}} \tag{4.3}$$

where R is the equilibrium radius. A change in radius is expected as the particles evolves from a square to a circle ($R^{circle} = \frac{2r^{square}}{\sqrt{\pi}}$). The equilibrium radius, dashed black line, is plotted as well as the expected final radius ,dashed red. Finally the compressibility of the fluid with respect to the surface tension coefficient γ is quantified . A square of size $0.2x0.2$ is evolved with $\gamma = 1, 0.1, 0.01$ the suggested range [3]. The difference in area of the initial square and the final circle is found and normalized with respect to the initial area.
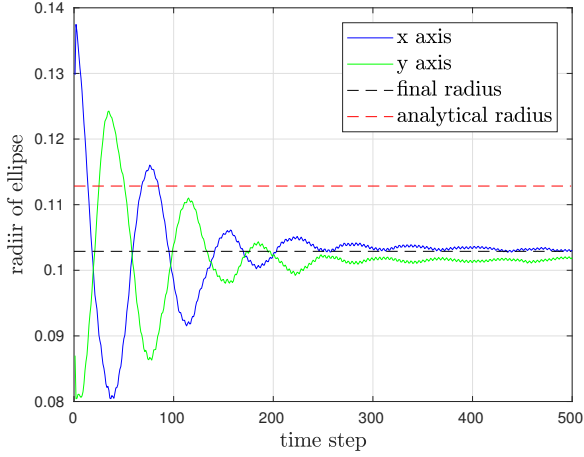
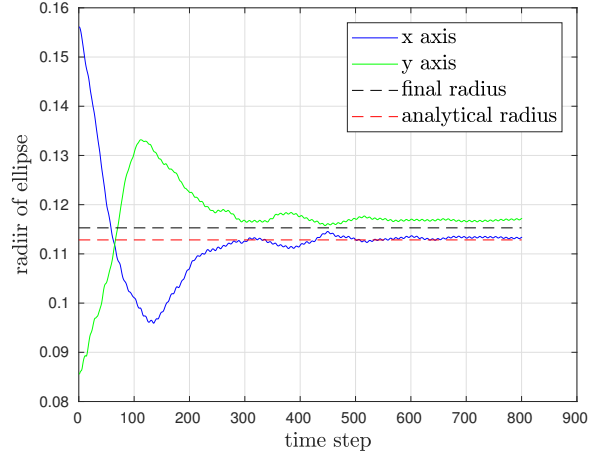**Figure 4.7:** Oscillation of Bubble deformed into an ellipse ($\Delta x = 0.01, \gamma = 1$)

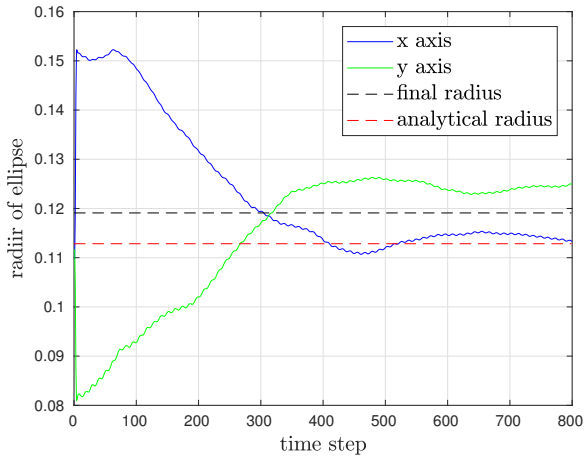**Figure 4.8:** Oscillation of Bubble deformed into an ellipse ($\Delta x = 0.01, \gamma = 0.1$)

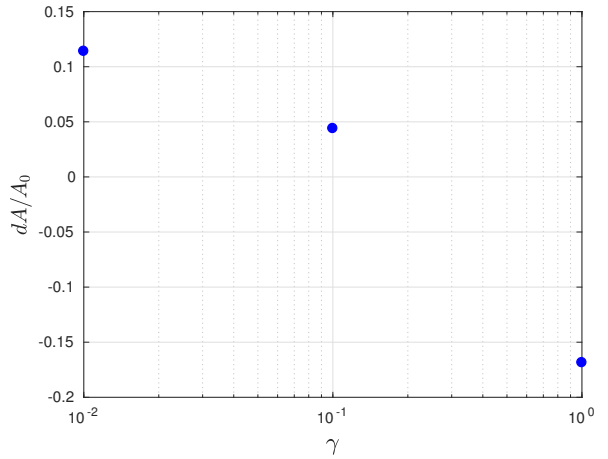**Figure 4.9:** Oscillation of Bubble deformed into an ellipse ($\Delta x = 0.01, \gamma = 0.01$)

Figure 4.10: Change in area of the liquid in square to bubble transformation

For a bubble with $\gamma = 1$ an oscillation period $\tau = 79$ is measured yielding the surface tension $\sigma = 0.0073$ (Fig.4.7). A video of this simulation can be found here. Figures 4.8 to 4.9 show that this method of measurement does not apply for liquids with lower surface tension coefficient. In this case, for the same density field and characteristic length, the *Weber* number of the flow has increased, thereby reducing the dominance of the cohesion forces. The flow becomes inertia dominated dampening the motion so that no oscillations are exhibited.

For $\gamma = 1$, the liquid is slightly compressed as the final radius is smaller than expected. For values of $\gamma < 1$, the compression effect disappears. This is investigated further as the compressibility ratio with

respect to γ, (Fig.4.10). Larger γ tends to compress the flow rather significantly. The SPH formulation alone is of the weakly compressible form. This would suggest a compressibility of 1%. The addition of the pairwise forces betrays this assumption as the fluid is being compressed by almost 17% for $\gamma = 1$. For smaller values of gamma, the effect is not so prominent.

The formulation of pairwise forces including the chosen model, are dependent on the discretization resolution. Figure 4.11 shows how the final pressure differs for a bubble of radius $R = 0.1$ with respect to a change in the prescribed inter particle distance (Δx) from which the volume of each particle is calculated ($V = \Delta x^2$). The pairwise forces dominate for this simulation and this is evident through testing of the density ratio, again confirming the compression effect that the pairwise force model has on the flow. The normalization term in front of the splines of both equations 3.5 and 3.7 are included to take care of this issue and keep change to a minimum for $\Delta x < 0.03$.
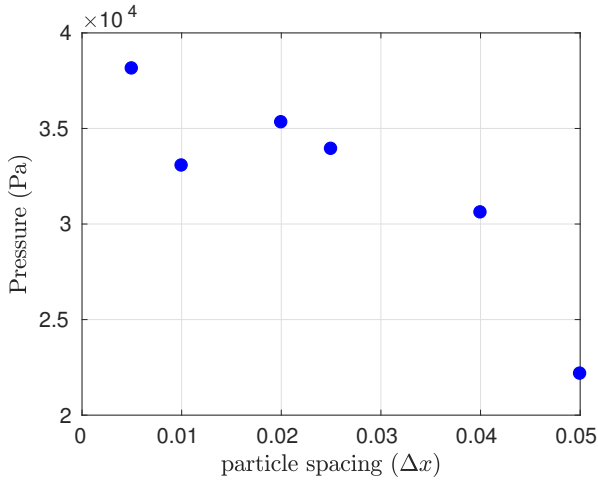

Figure 4.11: Sensitivity of the final pressure to particle spacing for a bubble of radius $R = 0.1$, $\gamma = 1$
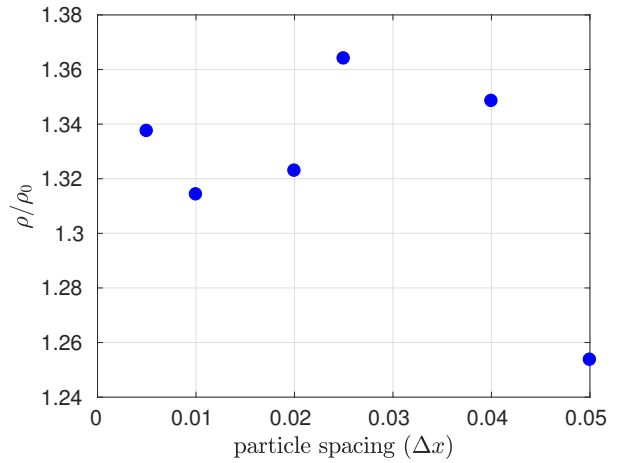
Figure 4.12: Sensitivity of the final density to particle spacing for a bubble of radius $R = 0.1$, $\gamma = 1$

4.2.2 Discussion

Both implementations, the PF alone and the PF and CSF together exhibit even particle distribution. A key attribute for maintaining accuracy in SPH simulations. A result of the negative force of the cohesion step wise continuous function for small inter-particle distance. The PF model alone exhibits a more even pressure distribution. The combination of forces seem to oscillate indefinitely even for long term simulations. However, it yields a linear relationship which obeys Laplaces equation (Fig.4.6). The oscillating bubble method of measuring the surface tension is not valid. The high density of the fluid means that even the strongest surface tension forces are quickly dampened. The value for surface tension $\sigma = 0.019064$ is taken, and is the reference value used to characterize the following test cases.

The compression effect of the pairwise forces, beyond that allowed by the WCSPH, must be addressed.
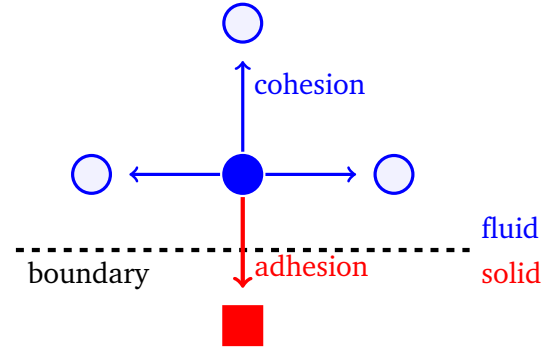
4.3 Solid wall Boundary Condition

The model exhibited non-physical separation which caused a drop on a flat surface to levitate and liquid in a tank to separate from the walls. The boundary condition used in the simulation is based on a force balance at the wall [2] . Thus it is necessary to add the the pairwise interaction for surface tension to the equilibrium. For a particle close to the wall, adhesion effects will dominate. We increase the pressure of the wall particle by an amount equivalent to the increase in pressure of the fluid particle due to the adhesion force. The force balance at the wall can be arrived by

$$\frac{dv_f}{dt} = -\frac{\Delta P_f}{\rho_f} + g + F^{adhesion} \qquad (4.4)$$

$$\int \Delta P \cdot dl = \rho_f \int (g + F^{adhesion}) \cdot dl \qquad (4.5)$$

$$p_w = p_f + \rho_f (g + F^{adhesion}) \cdot \mathbf{r}_{wf} \qquad (4.6)$$

Taking into account the contribution from all the particles within range of a wall particle yields

$$p_w = \frac{\sum pf\, W_{wf} + (g + F^{adhesion}) \sum \rho_f \mathbf{r}_{wf} W_{wf}}{\sum W_{wf}} \qquad (4.7)$$
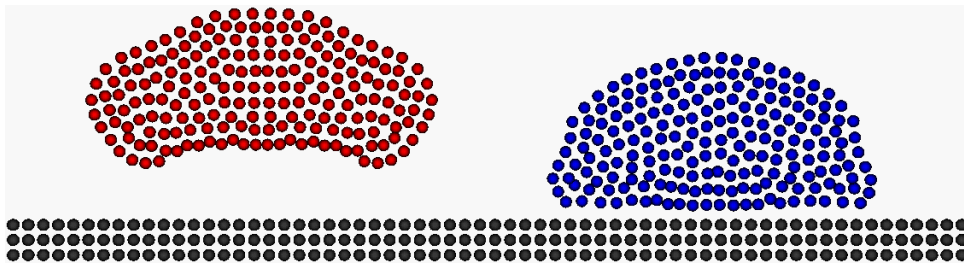

Figure 4.13: Drop without adapted boundary condition (red) exhibiting non-physical separation. Drop with adapted boundary condition (blue). At peak of separation. Click here for video.

4.4 Drops and Contact Angle

The aim of these simulations is to to confirm and calibrate the ability of the adhesion force to replicate different contact angles. These simulations are initialized as a rectangle on the surface with particle

spacing $\Delta x = 0.01$ in a Cartesian grid. The gravitational acceleration is that of earth $g_y = -9.81$, and the reference density for all the simulations which follow is $\rho_0 = 1000$. A no-slip boundary condition is prescribed. To avoid separation of the drop from the surface, the boundary condition adaptation is implemented. To find the contact angle for a SPH drop the surface is approximated by filtering the particles according to the color gradient $\mathbf{n}_a$ (Eqn. 3.6). The method captures the outermost layer of particles, which are define as the surface. The contact angle can be calculated by finding the angle of a line joining the root particle to other particles on the surface. The macroscopic nature of the simulation means that only the apparent contact angle is being measured.

The coefficients γ and β capture the behavior of the fluid with itself, and of the fluid with a rigid boundary respectively. The wetting of the liquid can therefore be controlled by a ratio of these parameters. Calibration for computational models is usually done through numerical experiments. Due to time constraints a more effective and accurate procedure was necessary. Tartakovsky and Pachenko have analytically derived relations between the coefficients of pure pairwise forces and macroscopic physical parameters, the contact angle and the surface tension [35]. These relations do not hold however when including the CS force as in the model here implemented. However, the suggested relations are used as a starting point for calibration with numerical experiments. Upon calibration it was found that the SPH coefficients can be related to a physical contact angle θ by

$$\gamma = 1 - \frac{3}{4}cos\theta \qquad (4.8) \qquad\qquad \beta = 1 + \frac{1}{2}cos\theta \qquad (4.9)$$

This contradicts Akinci's assertion that $0.001 \leq \gamma, \beta \leq 1$ [3], but the new range effectively models different contact angles and respects the new boundary condition.
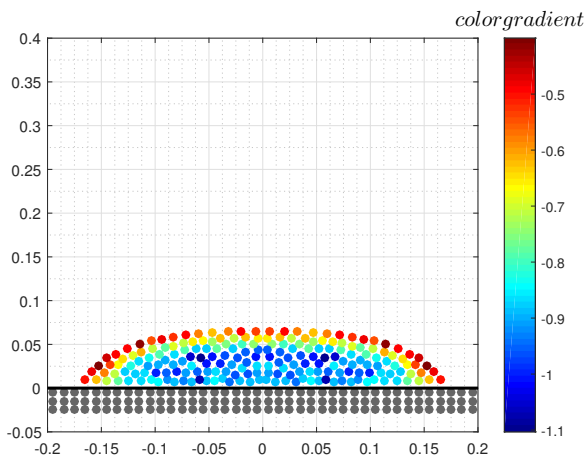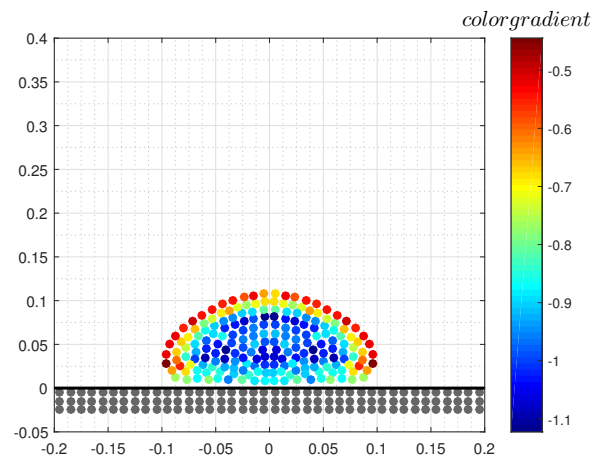

Figure 4.14: Prescribed contact angle $\theta = 30$

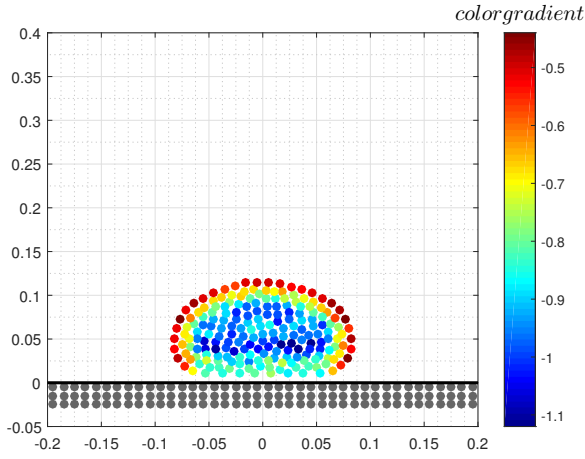**Figure 4.15:** Prescribed contact angle $\theta = 60$

Figure 4.16: Prescribed contact angle $\theta = 90$
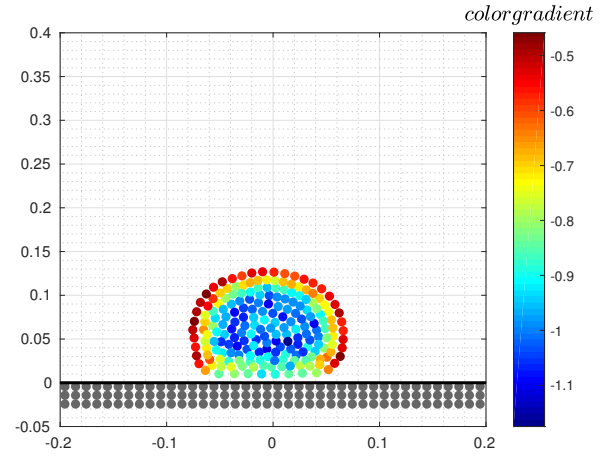

Figure 4.17: Prescribed contact angle $\theta = 120$

Similarly the contact angle can be visualized for a meniscus. The same relation for the surface tension coefficients holds. The simulation is initialized in a domain of width=1, height=0.5 and $\Delta x = 0.02$ yielding 1250 fluid particles. The fluid is evolved with varying cohesion and adhesion coefficients according to the contact angle. The non dimensional pressure is visualized.
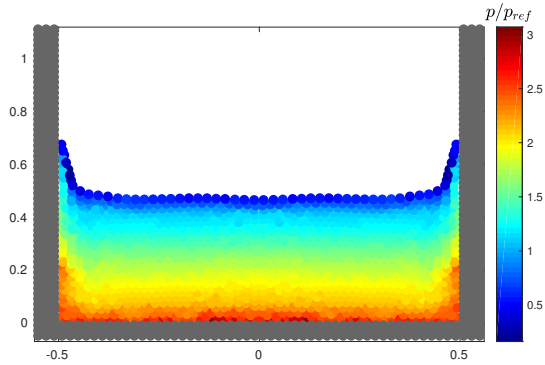

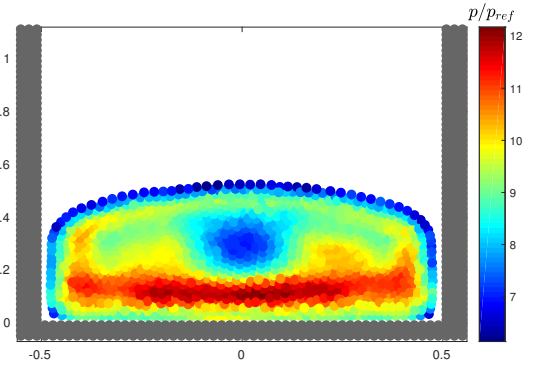**Figure 4.18:** Meniscus prescribed contact angle $\theta = 30$

Figure 4.19: Meniscus prescribed contact angle $\theta = 120$

4.4.1   Discussion

Two key features of variable contact angle are captured by this model. The liquid contracts reducing its wetting ability as the contact angle increases and the increase in height of the bubble, conserving mass. A second boundary condition would have to be prescribed in order to accurately capture the wetting effect, as even for wetting contact angles, the droplet exhibits hydrophobic behavior. For the meniscus the increase in contact angle and hence cohesion force, creates an non physical separation from the wall. The pressure distribution is also distorted for the hydrophobic case. For hydrophilic liquids, the meniscus is well captured. Both meniscus simulations over estimate the pressure.

4.5   Pressure Distribution

This section outlines the validation of the model for simulation of the hydrostatic test case. Previous work on this code had focused on achieving a perfect pressure distribution for the hydrostatic case [11]. It is imperative for the program to keep this characteristic.

4.5.1   Virial Pressure

Addition of the surface tension model to the SPH formulation over-estimates the hydrostatic pressure for high density fluids. Tartakovsky and Meakin [34] suggest a *Virial Pressure* in order to stabilize simulations for PF-SPH models. The virial theorem is based on an extra local pressure term due to interacting molecular forces. It suggests that the total pressure P cannot be calculated solely from the equation of state. Instead, addition of the contribution by molecular forces to the pressure from the equation of state P_k results in

$$P = P_k + \frac{1}{2dV} \sum_a \sum_b \mathbf{r}_{ab} \cdot \mathbf{F}_{ab} \tag{4.10}$$

for all particles a with neighboring particle b inside the volume V in a simulation with d dimensions. For the hydrostatic case, the virial pressure helps regulate the motion of the fluid. The virial pressure needs to be negative to guarantee stability. According to equation 4.10 our model is within this constraint as the pairwise force will have much larger magnitudes for particles near the interface, which are guaranteed to be negative.

4.5.2   Hydrostatic test case

The hydrostatic case the fluid is initialized in a Cartesian grid inside a container. The particle spacing is $\Delta x = 0.02$ yielding 2500 fluid particles. The pressure distribution is then compared to the analytical solution calculated by $p_{ref} = \rho_0 |g| \Delta y$. The gravitational strength of earth is used $g_y = -9.81$. For these simulations, the surface tension coefficients are set to $\gamma = \beta = 1$. The simulations are allowed to evolve for an extended period of non dimensional time $t_{ref} = H/v_{ref} = 10$. Eichstadt achieved a perfect pressure distribution for a liquid of density $\rho_0 = 1$ with an advanced diffusive term [11]. In this work, only the second order SPH correction known as the $\delta - SPH$ is implemented [5]. This density filtering method has been shown to be effective in stablizing flows with low Reynolds numbers and accurately captures the hydrostatic case. We simulate fluids of density $\rho_0 = 1$ and $\rho_0 = 1000$ to verify the formulation holds for a variety of fluids.
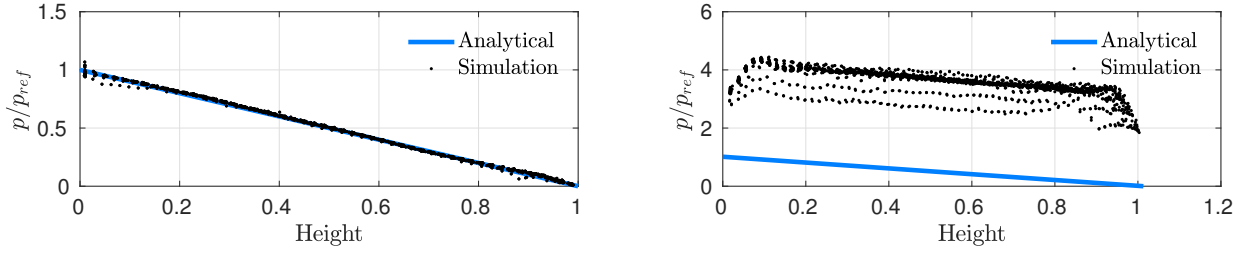
Figure 4.20: Comparison of simulated pressure distribution to analytical pressure distribution $\rho = 1$ (left) $\rho = 1000$ (right)
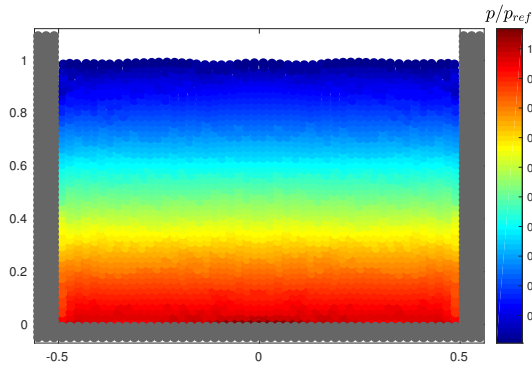

Figure 4.21: Hydrostatic test case including the surface tension model with virial pressure $\rho = 1, \Delta x = 0.02, \gamma = \beta = 1$

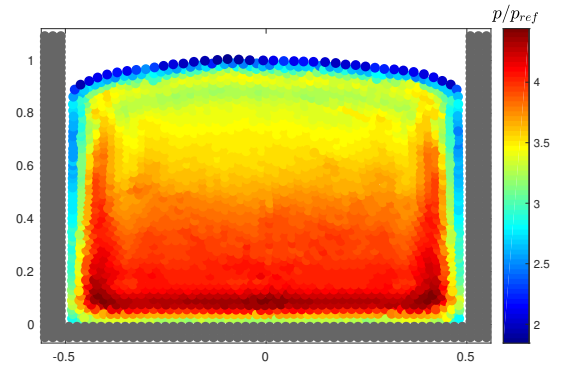**Figure 4.22:** Hydrostatic test case including the surface tension model with virial pressure $\rho = 1000, \Delta x = 0.02, \gamma = \beta = 1$

4.5.3 Discussion

Figure 4.21 depicts a fluid of density $\rho = 1$ with the added virial pressure. The pressure distribution is as expected and satisfies the analytical solution (Fig.4.20(left)). In this case, the virial pressure has had an almost neglegible effect. The only major variation is near the surface which is where the capillary effects are dominant. The density filtering method is not affected by the surface tension model implemented. Although at the bottom of the tank, the pressure remains slightly over estimated. For the fluid with increased density however, a meniscus, characteristic of dense liquids has been captured (Fig.4.22). In this case, the surface tension terms have clearly been dominant as the entire perimeter of the liquid seems to have an underestimated pressure, a feature due to the internal direction of the cohesion forces. In general, the pressure has been overestimated with respect to the analytical solution(Fig.4.20(right)) and hence we assume that the virial pressure has not achieved the desired outcome. Careful consideration should be given to the inaccuracy exhibited due to an increase in reference density.

4.6 Water Crown

To test how the model behaves in dynamic conditions, splashing is simulated. Upon impact the splash will form a coherent liquid structure often called the "liquid crown", "milk crown" or the "aquafina crown". A liquid drop of radius $r = 0.1$ is initialized at a height 0.6 above a tank of width 0.8 and depth 0.4 filled with the same fluid. The bubble is initialized with a velocity in the negative y direction of $5m/s$. A concentric circle initialization is necessary for the bubble to ensure that for the same resolution Δx and the same reference density ρ_0 the liquid in the drop is the same as the liquid in the tank. A particle spacing of $\Delta x = 0.02$ yields 1750 liquid particles. The gravitational acceleration is set to $g = 9.81$ in the negative y-direction. The simulation is allowed to evolve from its initial configuration (Fig.4.23). It has been found that there are two non-dimensional numbers which characterize the drop impact on liquid film, the drop Weber number $We_{drop} = \rho v^2 d/\sigma$ and the inertia ratio $\zeta = d/h$ where d is the drop diameter and h is the liquid film thickness. For a fluid with $\rho_0 = 1000$, $We_{drop} = 131137$ and $\zeta = 0.5$.
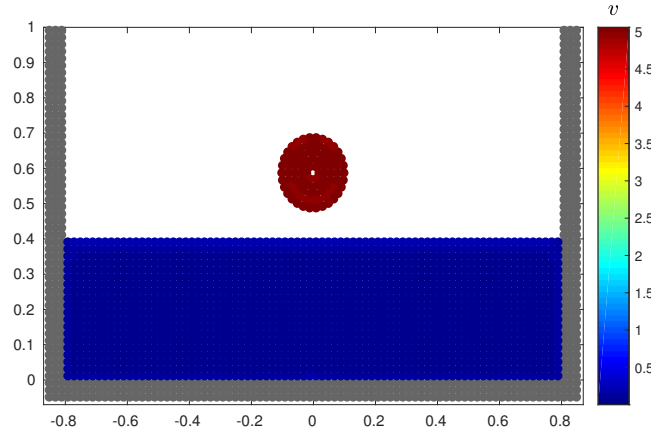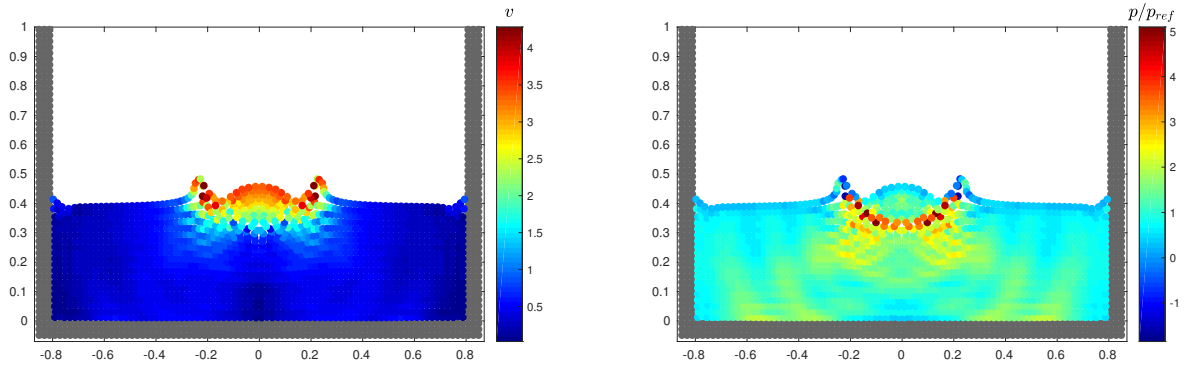

Figure 4.23: Initial configuration for crown formation simulation. static liquid in blue, drop with prescribed velocity in red
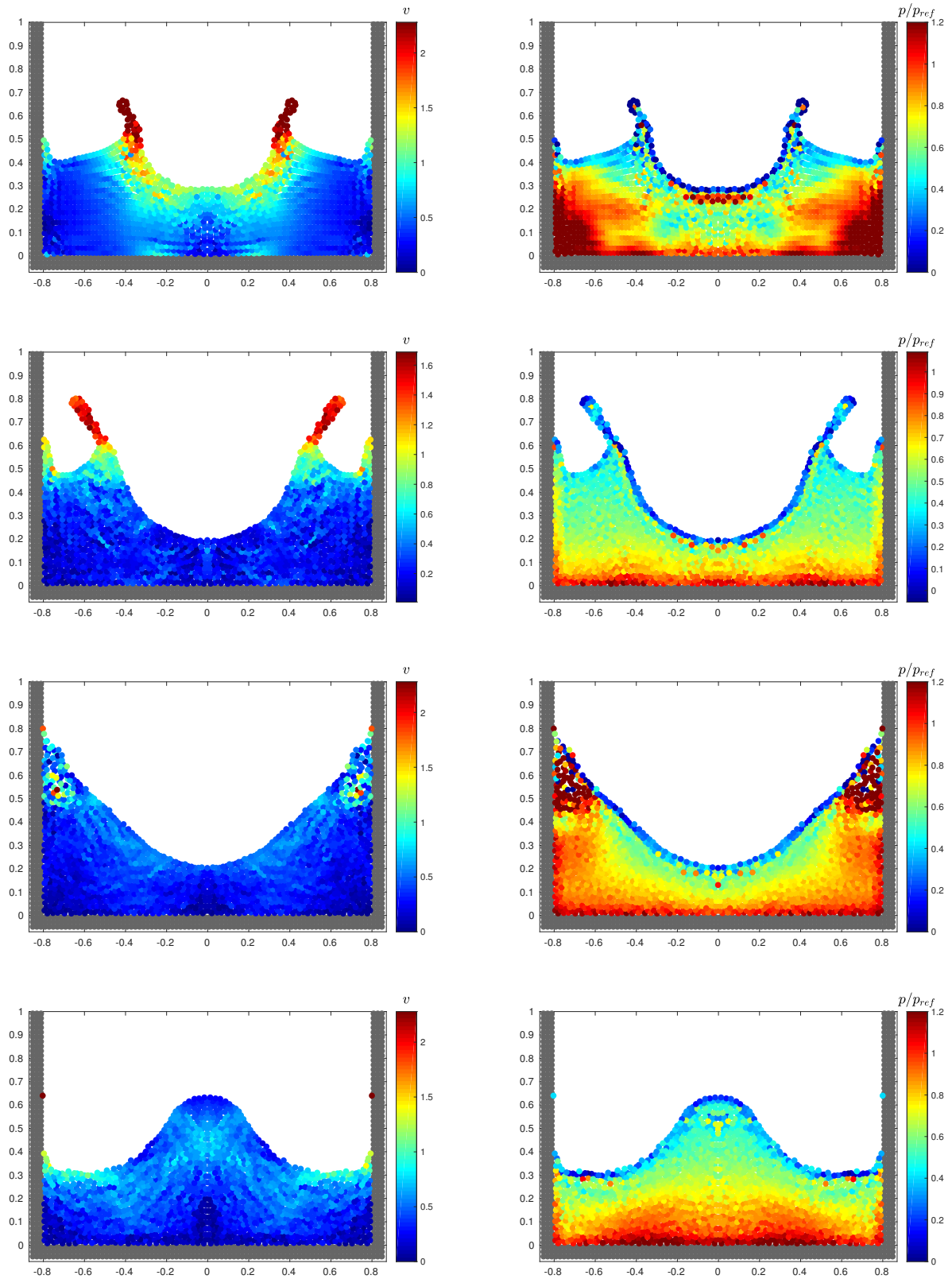
Figure 4.24: A video of this simulation is captured visualizing the velocity and the pressure

To validate this model for violent motion, the results are compared against the experimentally derived power law dependence of the non-dimensional cavity radius on the non-dimensional time [39]. In the analytical derivation of the law, the crown formation is treated as a kinematic discontinuity and the drop impact is represented by a steep parabolic perturbation in the velocity field. A derivation of this form is followed and generalized to the two dimensional planar case by Roismann and Tropea where it is shown that the same power law applies [30]. That is, in a cylindrical coordinate system, the propagation of the crown is also proportional to the square root of non-dimensional time.

$$\frac{r}{D} = k\hat{t}^{1/2} \tag{4.11}$$

where r is the radius of the cavity, D is the diameter of the drop, and $\hat{t}$ is non-dimensional time per $\hat{t} = tV/D$, where V is the impact velocity. The base of the crown is defined at the maximum height of the fluid film before impact. The evolution of the base radius r_b is recorded by setting a series of material point at height 0.4 and performing a nearest neighbor search at each time frame. The radius of the base is then the first particle found within h of a material point. The crown radius, r_c, is defined at the maximum height of every frame in the positive x half of the domain.
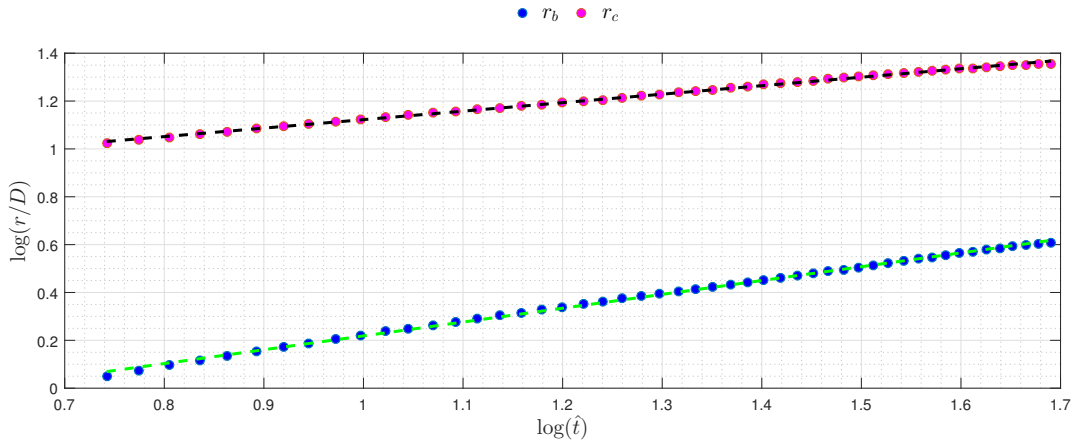

Figure 4.25: Evolution of base radius and crown radius in non-dimensional units ($\hat{t}$).

The theory suggests proportionality to the square root of non-dimensional time which in this case is 0.4657. The evolution of the crown formation is measured as the slope of a regression of the *log* of the evolution of the radial distance (Fig.4.25), which yields 0.4665, very close to the expected value. Experiments have shown that the ejecta, which eventually forms the crown, comes from the fluid film. This can be captured using a finer particle resolution ($\Delta x = 0.01$) and assigning different colors to the drop (green) and the film (blue) fluids. For a larger rise of the crown and hence a clearer difference as of the source of the crown fluid, a thin film of depth 0.2 is used. In video format, the ability to differentiate the particles helps to track how the particles in the bubble disperse.
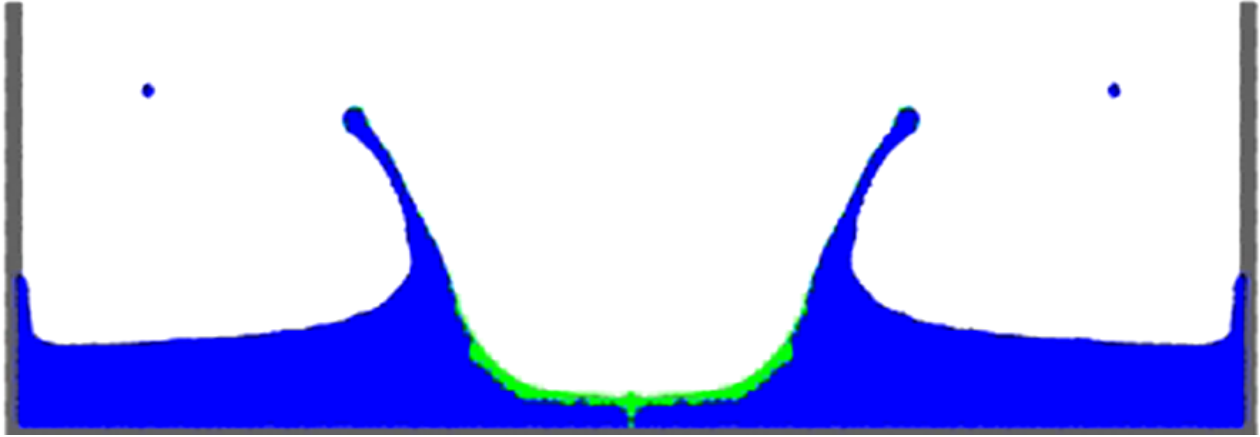
Figure 4.26: Crown formation of a drop on a thin film showing that the crown forms from the ejecta. Drop particles in green, film particles in blue. A video can be found here

4.6.1 Discussion

Even under violent motion, the coherent structures are well captured with the chosen model. Immediately after formation of the ejecta, surface tension forces form the coherent structure called the *liquid crown*.The adhesion of a fluid particles to the wall upon splashing is reminiscent of drop on a surface slowly moving under the force of gravity. Due to the small particle neighborhood though, the properties of the drop are not well estimated and fluctuate rapidly at each time step. The simulation is true to the theoretical analysis in following the power law for the evolution of the crown. The radial evolution of the crown with a similar rate as the cavity is confirmed. The crown then collapses as it loses momentum and the capillary and inertial forces are taken over by body forces.

$\sqrt{\hat{t}}$	0.4657
average slope	0.4665

Table 4.1: results from the power law evolution of the crown

Fig. 4.26 reveals the effects of reducing the film thickness. The proportionality of the rise of the crown to the thickness of the film is obvious if momentum in the vertical direction is to be conserved. A positive feature highlighted by the smaller particle size is the formation of a drop at the peak of the crown upon bifurcation from the liquid mass. Even for a small particle neighborhoods, the cohesive forces maintain the macroscopic geometry of the drop. The simulation is true to experimental findings that the source of the crown is the initially stationary fluid film, and not from the drop itself.

5. Conclusion and Future Work

In conclusion, a suitable model was chosen and successfully implemented into the SPH program. It effectively replicates the key characteristics of surface tension necessary.

Representing the surface tension dynamics which are of molecular nature can be simply done in SPH with pairwise forces under isomorphism with molecular dynamics. Although this implementation is not strictly of the form, it proved to be valid as the simulations are faithful to the theory, both Laplaces equation and the crown evolution power law are followed.

Issues remain for rigid-fluid interaction when the surface tension force is added. This authors adaptation of the boundary condition by Adami et al. alleviates the issue of non physical separation of the fluid from the wall in the drop test case. However, it does not perform for vertical walls or boundaries with more complex geometries.

With respect to the liquid contact angle, the implementation presented is effective in replicating different wetting conditions. While several attempts at relating the SPH surface tension coefficients to a physical contact angle were made this should continue as a more accurate formulation is desired. Much progress has been made towards this most recently by Tartakovsky and Pachenko for pure pairwise force models [35]. The framework which Tartakovsky et al. build for relating the coefficients of pairwise forces to macroscopic physical variables is analytically derived. However, for this model it underestimates the strength of the cohesive force as the liquid systematically exhibited a larger contact angle then prescribed. Thus An extension to the combined PF and CSF model is necessary.

The dampening of the motion in the oscillatory bubble test case highlights one of the issues with implementing a pairwise force model with this particular SPH formulation. The equation of motion discretized is the Euler equations which are inviscid. In this respect, there should be no force to dissipate the motion of the bubble. SPH requires a numerical dissipation in order to stabilize the scheme and avoid spurious numerical effects. Further, the viscosity term here used (Eqn.2.5) adds a contribution to the viscous forces only for the particles which are moving towards each other. The PF model is based on adding an acceleration between particles which would cause a velocity towards one another, in this respect, the viscous force will be overactive. A possible solution would be a criterion for implementation of viscosity based on forces.

Finally, the parallelization of this code has aided in the rapid development of this model. Maintaining this parallelization and optimizing the costly CSF functions was a key goal in this work which was achieved.

33

Future work should include testing of a different formulation for the Euler equation which fully satisfies the conditions in the isomorphism argument for the continuum representation of surface tension as a pairwise force. The currently implemented form of the pressure term is said to be better for multi-fluid simulations [11]. However, it is this authors opinion that a formulation that is truly isomorphic to molecular dynamics could aid in the addition of further physical phenomena, the next key step of which would be temperature. The isothermal nature of the current code fails to take into account the variation of surface tension with temperature.

Changes in surface tension strength along the surface which may cause spurious currents could be added by adopting a more complex model based on the stress tensor at the liquid surface. This would also aid in post-processing for measurement of the free surface energy, a better measure of convergence for the free bubble test case. The continuum nature of SPH fails to capture the microscopic behavior of the contact line causing hydrophobic like behavior only. Advances in adaptive and local refinement for SPH together with matching of molecular dynamics could accurately simulate contact line dynamics for a large range of capillary numbers. Success would avoid the contact line singularity of the continuum description currently present.

Further validation of the code for test cases involving multi-fluids are also suggested. The Kevin-Helmholtz instability is a prime candidate which rigorously tests much of the implemented work so far and for which there is validation tests made available by SPHERIC.

In this codes aim to replicate sloshing under compensated gravity, numerical experiments should be carried out under those conditions. Access to the recently gathered long term data flow from SPEHERES-Slosh could eventually be used for calibration of this code.

Finally, to facilitate further development of the program, a flowchart of the program's current structure is included. MATLAB is the language employed which can often become complex to understand due to the fact that it is based on functions. The flowchart will allow future developers to quickly understand the relations between these functions.
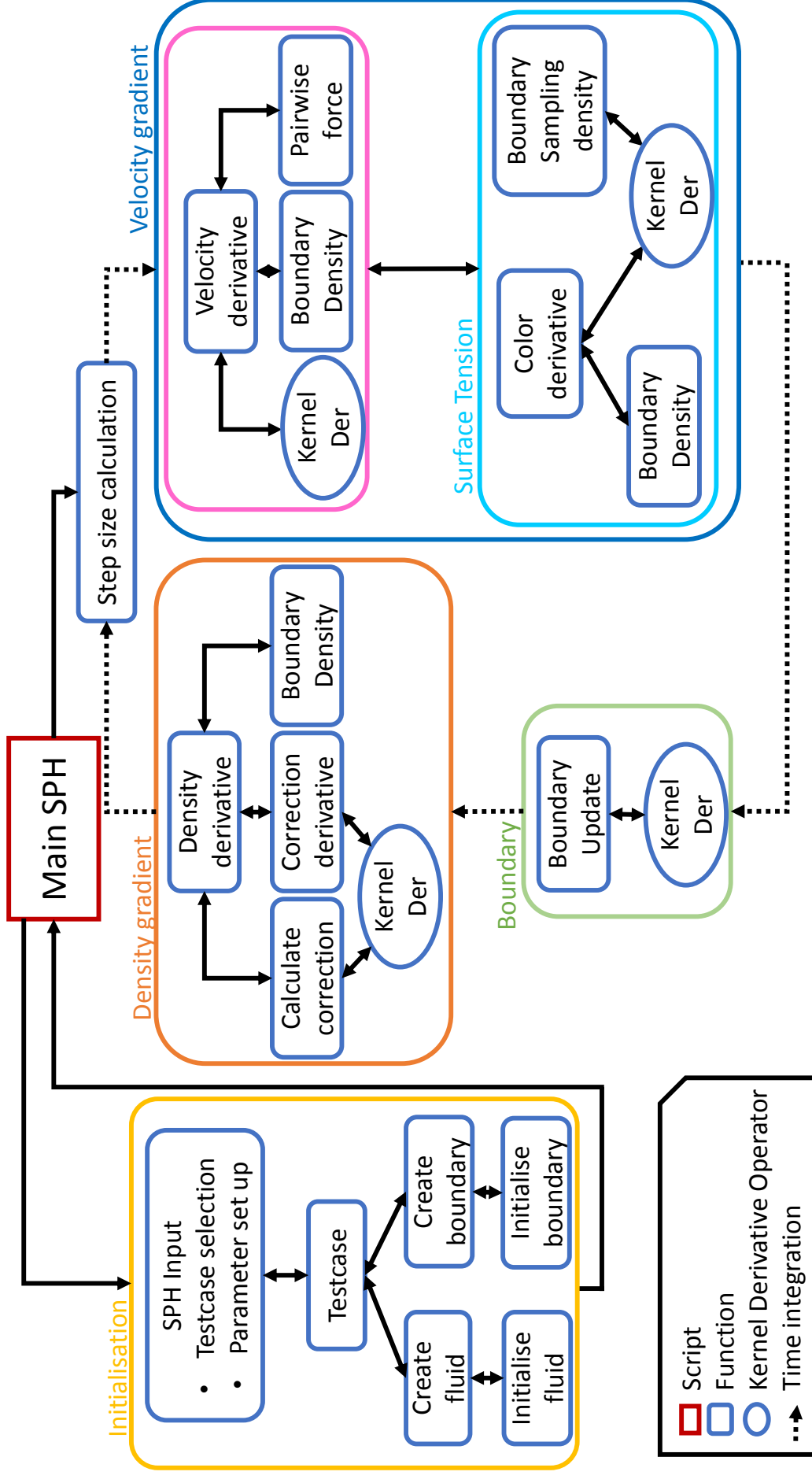
Bibliography

[1] S. Adami, X. Hu, and N. Adams. A conservative SPH method for surfactant dynamics. *Journal of Computational Physics*, 229(5):1909–1926, 2010.

[2] S. Adami, X. Hu, and N. Adams. A generalized wall boundary condition for smoothed particle hydrodynamics. *Journal of Computational Physics*, 231(21):7057–7075, 2012.

[3] N. Akinci, G. Akinci, and M. Teschner. Versatile surface tension and adhesion for SPH fluids. *ACM Transactions on Graphics (TOG)*, 32(6):182, 2013.

[4] N. Akinci, M. Ihmsen, G. Akinci, B. Solenthaler, and M. Teschner. Versatile rigid-fluid coupling for incompressible SPH. *ACM Transactions on Graphics (TOG)*, 31(4):62, 2012.

[5] M. Antuono, A. Colagrossi, and S. Marrone. Numerical diffusive terms in weakly-compressible sph schemes. *Computer Physics Communications*, 183(12):2570–2580, 2012.

[6] U. Bandara, A. M. Tartakovsky, M. Oostrom, B. J. Palmer, J. Grate, and C. Zhang. Smoothed particle hydrodynamics pore-scale simulations of unstable immiscible flow in porous media. *Advances in Water Resources*, 62:356–369, 2013.

[7] L. Brubb and D. A. Petrash. Experimental investigation of interfacial behavior following termination of outflow in weightlessness. 1967.

[8] A. Colagrossi. A meshless lagrangian method for free-surface and interface flows with fragmentation. *PhD Thesis, Universita di Roma*, 2005.

[9] P.-G. De Gennes, F. Brochard-Wyart, and D. Quéré. *Capillarity and wetting phenomena: drops, bubbles, pearls, waves*. Springer, 2013.

[10] M. Dreyer. *Free surface flows under compensated gravity conditions*, volume 221. Springer, 2007.

[11] J. Eichstadt. Modelling of sloshing using smooth particle hydrodynamics. *MSc Thesis, Department of Aeronautics, Imperial College London*, 2014.

[12] M. Ferrand, D. Laurence, B. D. Rogers, D. Violeau, and C. Kassiotis. Unified semi-analytical wall boundary conditions for inviscid, laminar or turbulent flows in the meshless SPH method. *International Journal for Numerical Methods in Fluids*, 71(4):446–472, 2013.

[13] B. Godderidge, S. Turnock, M. Tan, and C. Earl. An investigation of multiphase CFD modelling of a lateral sloshing tank. *Computers & Fluids*, 38(2):183 – 193, 2009.

[14] W. G. Hoover and S. Hess. Equilibrium and nonequilibrium thermomechanics for an effective pair potential used in smooth particle applied mechanics. *Physica A: Statistical Mechanics and its Applications*, 231(4):425–438, 1996.

[15] X. Y. Hu and N. A. Adams. A multi-phase SPH method for macroscopic and mesoscopic flows. *Journal of Computational Physics*, 213(2):844–861, 2006.

[16] M. Huber, S. Reinhardt, D. Weiskopf, and B. Eberhardt. Evaluation of surface tension models for SPH-based fluid animations using a benchmark test. In *VRIPHYS*, pages 41–50, 2015.

[17] R. A. Ibrahim, V. Pilipchuk, and T. Ikeda. Recent advances in liquid sloshing dynamics. *Applied Mechanics Reviews*, 54(2):133–199, 2001.

[18] M. Ihmsen, N. Akinci, M. Gissler, and M. Teschner. Boundary handling and adaptive time-stepping for PCISPH. In *Workshop on virtual reality interaction and physical simulation VRIPHYS*, 2010.

[19] J. Kordilla, A. M. Tartakovsky, and T. Geyer. A smoothed particle hydrodynamics model for droplet and film flow on smooth and rough fracture surfaces. *Advances in Water Resources*, 59:1–14, 2013.

[20] G. Lapilli, D. R. Kirk, H. Gutierrez, P. Schallhorn, B. Marsell, J. Roth, and J. Moder. Results of microgravity fluid dynamics captured with the SPHERES-Slosh experiment. 2015.

[21] S. Li and W. K. Liu. Meshfree and particle methods and their applications. *Applied Mechanics Reviews*, 55(1):1–34, 2002.

[22] J. J. Monaghan. Smoothed particle hydrodynamics. *Annual review of astronomy and astrophysics*, 30(1):543–574, 1992.

[23] P. Nair and T. Poeschel. Surface tension and wetting phenomena using incompressible SPH. *arXiv preprint arXiv:1701.02672*, 2017.

[24] S. Nugent and H. Posch. Liquid drops and surface tension with smoothed particle applied mechanics. *Physical Review E*, 62(4):4968, 2000.

[25] D. A. Petrash, T. M. Nelson, and E. W. Otto. *Effect of surface energy on the liquid-vapor interface configuration during weightlessness*. NASA-TN-D-1582, 1963.

[26] D. A. Petrash, R. C. Nussel, and E. W. Otto. *Effect of the acceleration disturbances encountered in the MA-7 spacecraft on the liquid-vapor interface in a baffled tank during weightlessness*. NASA-TN-D-1577, 1963.

[27] D. A. Petrash, R. C. Nussle, and E. W. Otto. *Effect of contact angle and tank geometry on the configuration of the liquid-vapor interface during weightlessness*, volume 2075. NASA-TN-D-2075, 1963.

[28] D. A. Petrash, R. F. Zappa, and E. W. Otto. Experimental study of the effects of weightlessness on the configuration of mercury and alcohol in spherical tanks. Technical report, NASA-TN-D1197, 1962.

[29] S. Rebouillat and D. Liksonov. Fluid-structure interaction in partially filled liquid containers: A comparative review of numerical approaches. *Computers and Fluids*, 39(5):739 – 746, 2010.

[30] I. Roisman and C. Tropea. Impact of a drop onto a wetted wall: description of crown formation and propagation. *Journal of Fluid Mechanics*, 472:373–397, 2002.

[31] R. Scardovelli and S. Zaleski. Direct numerical simulation of free-surface and interfacial flow. *Annual review of fluid mechanics*, 31(1):567–603, 1999.

[32] J. A. Sethian and P. Smereka. Level set methods for fluid interfaces. *Annual Review of Fluid Mechanics*, 35(1):341–372, 2003.

[33] M. Shadloo, G. Oger, and D. Le Touzé. Smoothed particle hydrodynamics method for fluid flows, towards industrial applications: Motivations, current state, and challenges. *Computers & Fluids*, 136:11–34, 2016.

[34] A. Tartakovsky and P. Meakin. Modeling of surface tension and contact angles with smoothed particle hydrodynamics. *Physical Review E*, 72(2):026301, 2005.

[35] A. M. Tartakovsky and A. Panchenko. Pairwise force smoothed particle hydrodynamics model for multiphase flow: Surface tension and contact line dynamics. *Journal of Computational Physics*, 305:1119 – 1146, 2016.

[36] D. Violeau. *Fluid Mechanics and the SPH method: theory and applications*. Oxford University Press, 2012.

[37] Z.-B. Wang, R. Chen, H. Wang, Q. Liao, X. Zhu, and S.-Z. Li. An overview of smoothed particle hydrodynamics for simulating multiphase flow. *Applied Mathematical Modelling*, 40(2324):9625 – 9655, 2016.

[38] W.G.Hoover. *Smoothed Particle Applied Dynamics - The state of the art*. World Scientific, Volume 25 of the advanced series in nonlinear dynamics, 2006.

[39] A. Yarin and D. Weiss. Impact of drops on solid surfaces: self-similar capillary waves, and splashing as a new type of kinematic discontinuity. *Journal of Fluid Mechanics*, 283:141–173, 1995.